## ARTICLE

Check for updates

# High-specific-power flexible transition metal dichalcogenide solar cells

Koosha Nassiri Nazif [1,8], Alwin Daus[1,8], Jiho Hong [2,3], Nayeun Lee[2,3], Sam Vaziri[1], Aravindh Kumar [1], Frederick Nitta[1], Michelle E. Chen [3], Siavash Kananian [1], Raisul Islam[1], Kwan-Ho Kim[4,5], Jin-Hong Park [4,6], Ada S. Y. Poon [1], Mark L. Brongersma [2,3,7], Eric Pop [1,3] & Krishna C. Saraswat [1,3 ✉]

Semiconducting transition metal dichalcogenides (TMDs) are promising for flexible high-specific-power photovoltaics due to their ultrahigh optical absorption coefficients, desirable band gaps and self-passivated surfaces. However, challenges such as Fermi-level pinning at the metal contact–TMD interface and the inapplicability of traditional doping schemes have prevented most TMD solar cells from exceeding 2% power conversion efficiency (PCE). In addition, fabrication on flexible substrates tends to contaminate or damage TMD interfaces, further reducing performance. Here, we address these fundamental issues by employing: (1) transparent graphene contacts to mitigate Fermi-level pinning, (2) $MoO_x$ capping for doping, passivation and anti-reflection, and (3) a clean, non-damaging direct transfer method to realize devices on lightweight flexible polyimide substrates. These lead to record PCE of 5.1% and record specific power of 4.4 W g$^{-1}$ for flexible TMD ($WSe_2$) solar cells, the latter on par with prevailing thin-film solar technologies cadmium telluride, copper indium gallium selenide, amorphous silicon and III-Vs. We further project that TMD solar cells could achieve specific power up to 46 W g$^{-1}$, creating unprecedented opportunities in a broad range of industries from aerospace to wearable and implantable electronics.

[1] Department of Electrical Engineering, Stanford University, Stanford, CA 94305, USA. [2] Geballe Laboratory for Advanced Materials, Stanford University, Stanford, CA 94305, USA. [3] Department of Materials Science and Engineering, Stanford University, Stanford, CA 94305, USA. [4] Department of Electrical and Computer Engineering, Sungkyunkwan University, Suwon 16419, Korea. [5] Department of Electrical and Systems Engineering, University of Pennsylvania, Philadelphia, PA 19104, USA. [6] SKKU Advanced Institute of Nanotechnology (SAINT), Sungkyunkwan University, Suwon 16419, Korea. [7] Department of Applied Physics, Stanford University, Stanford, CA 94305, USA. [8] These authors contributed equally: Koosha Nassiri Nazif, Alwin Daus. ✉email: saraswat@stanford.edu

Conventional silicon (Si) solar cells dominate the photo-voltaics market with a market share of about 95% due to their low-cost manufacturing and reasonable power conversion efficiency (PCE)[1]. However, the low optical absorption coefficient and brittle nature of Si lead to degraded performance in ultrathin, flexible Si solar cells and therefore prevent their broader usage in applications demanding high power per weight (i.e., specific power, $P_S$) and flexibility, for example in aerospace, transportation, architecture, and self-powered wearable and implantable electronics[2–10].

Emerging semiconducting transition metal dichalcogenides (TMDs) exhibit excellent properties for such flexible high-specific-power photovoltaics. These include ultrahigh optical absorption coefficients up to one order of magnitude greater than conventional direct bandgap semiconductors, near-ideal band gaps for solar energy harvesting, and self-passivated surfaces[11–18]. In fact, ultrathin (<20 nm) TMDs can achieve near-unity, broadband, and omnidirectional absorption in the visible spectrum[15,16]. The wide range of TMD band gaps (~1.0–2.5 eV)[17] are also well suited for highly efficient single-junction or double-junction tandem solar cells[13]. In addition, the dangling-bond-free surfaces of layered TMDs enable heterostructures without the constraint of lattice matching, offering abundant design choices for TMD photovoltaics[18]. According to realistic detailed balance models[13], a PCE of ~27% can be achieved in ultrathin single-junction TMD solar cells, leading to extremely high $P_S$ once implemented on lightweight flexible substrates[8].

Despite these promising forecasts, there have not been any such demonstrations due to difficulties in reaching high PCE and integrating materials on flexible substrates. The PCE of TMD solar cells has typically not exceeded 2%[19–25], mostly due to strong Fermi-level pinning at the metal contact–TMD interface[26] and the inapplicability of traditional doping schemes such as diffusion or ion implantation, which can damage TMDs[27]. Reducing or eliminating Fermi-level pinning by adopting a gentle metal transfer method[22,26], introducing an ultrathin interlayer at the metal–TMD interface[28–31], or forming a van der Waals (vdW) heterojunction such as graphene-TMD[32–34] can significantly improve the performance of TMD devices. In addition, forming a p–n homojunction by employing TMD-compatible doping methods such as surface charge transfer and fixed charge doping via metal oxides[23–25], plasma doping[35], or electrostatic doping[36] has been shown to enhance the photovoltaic performance. Noteworthily, the highest PCEs in thin-film single-junction TMDs are 2.8% in plasma-doped $MoS_2$ and 6.3% in electrostatically-doped $MoSe_2$ solar cells[35,36]. At the same time, TMDs are typically transferred to flexible substrates and most of these processes can damage TMD interfaces, leave unwanted polymer residues, and do not allow for a reliable and practical vertical device architecture[37]. Previous reports on $P_S$ of TMD solar cells, i.e., 3 W g$^{-1}$ with a PCE of 0.46%[22] and 2500 W g$^{-1}$ with a PCE of 1.0%[14], do not account for the substrate's weight, which practically constitutes the largest part of the overall weight and needs to be considered for accurate $P_S$ calculations. The only TMD solar cell on a lightweight, flexible substrate reported to date has a PCE of <0.7%, yielding a $P_S$ of <0.04 W g$^{-1}$ [20].

Here, we address the above-mentioned device and integration challenges by utilizing transparent graphene contacts mitigating Fermi-level pinning, $MoO_x$ capping for doping, passivation and anti-reflection coating, and a clean, non-damaging direct transfer method to realize TMD solar cells for the first time on an ultrathin (5 μm), lightweight and flexible polyimide (PI) substrate. The flexible TMD ($WSe_2$) solar cells made in this fashion achieve a PCE of 5.1%, surpassing previous flexible TMD solar cells by more than an order of magnitude[20]. Furthermore, the integration on an ultrathin substrate enables a $P_S$ of 4.4 W g$^{-1}$, more than 100× higher than previous results on flexible TMD photovoltaics[20] and in the same range as champion solar cells of prevailing thin-film technologies cadmium telluride (CdTe), copper indium gallium selenide (CIGS), amorphous silicon (a-Si) and group III–V semiconductors[38–45]. In future, TMD solar cells on even thinner substrates and with higher PCEs could potentially achieve an unprecedented $P_S$ of ~46 W g$^{-1}$ (as we project in this work) opening up far-reaching possibilities in a broad range of industries[9].

## Results and discussion

**Design and fabrication of flexible WSe$_2$ solar cells.** We fabricate flexible vertical photovoltaic cells from multilayer (~200 nm) tungsten diselenide ($WSe_2$) absorbers, transparent hole-collecting graphene top contacts covered by $MoO_x$ doping, passivation and anti-reflection coatings, and optically-reflective electron-collecting gold (Au) bottom contacts. The bottom contact and absorber material are embedded into a flexible, transparent polyimide substrate. Device schematics and optical images are shown in Fig. 1a–d. We mechanically exfoliate $WSe_2$ flakes on thermally oxidized silicon substrates and deposit patterned Au bottom contacts, which are all covered with spin-coated polyimide and released together in deionized water[46]. The patterned transparent top contacts constituted of graphene and $MoO_x$ are then formed on top via graphene wet transfer and $MoO_x$ electron-beam (e-beam) evaporation. Details on device fabrication and transfer procedures can be found in Supplementary Note 1 and Supplementary Fig. 1.

Figure 1e shows the schematic energy band diagram of flexible $WSe_2$ solar cells based on energy levels of $WSe_2$, graphene (Gr), and Au reported in the literature. $WSe_2$ has a bulk band gap of ~1.2 eV and electron affinity of ~4.0 eV[21,47–49], and is undoped according to the bulk crystal vendor. Due to the energetic nature of e-beam evaporation, defect states are induced at the Au–WSe$_2$ interface, and the Au Fermi level is pinned toward the charge neutrality level of $WSe_2$ located around midgap[26,50,51]. This decreases the effective work function of Au and makes it a decent electron-collecting contact. We find that replacing Au with lower work function metals such as Ti and Al leads to a lower performance, most probably due to their reactive nature therefore forming poor interfaces with $WSe_2$ (Supplementary Fig. 2)[52]. On the other hand, layered materials Gr and $WSe_2$ experience no Fermi-level pinning at their vdW interface[32–34]. The work function of undoped graphene is ~4.6 eV (e.g., in vacuum), which increases to ~5.0 eV when graphene is exposed to air[53–55]. Graphene and the undoped $WSe_2$, therefore, form a Schottky junction with a hole barrier height of 0.1–0.2 eV and a built-in potential of 0.4–0.5 eV[33,34,56]. The $MoO_x$ on top further p-dopes graphene, increasing its work function and therefore the built-in potential of the Gr–WSe$_2$ Schottky junction by ~0.16 eV (Supplementary Note 2, Supplementary Table 1 and Supplementary Fig. 3a, b). $MoO_x$ also passivates the top surface of the solar cell, specifically the trap states at the Gr–WSe$_2$ interface[24]. These lead to a higher open-circuit voltage ($V_{OC}$) and short-circuit current density ($J_{SC}$) in $MoO_x$-capped $WSe_2$ solar cells (Supplementary Note 2 and Supplementary Fig. 3c). As we will discuss later in the optical characterization section, $MoO_x$ also serves as an effective anti-reflection coating for $WSe_2$, leading to an additional increase in $J_{SC}$. Given the approximate locations of Gr, $WSe_2$, and Au Fermi levels, the depletion regions of Gr–WSe$_2$ and Au–WSe$_2$ Schottky junctions are estimated to be in the order of 1 μm and therefore expand throughout the entire depth of the ~200-nm-thick $WSe_2$ layer, leading to fully depleted devices with a built-in potential of ~0.6 eV.
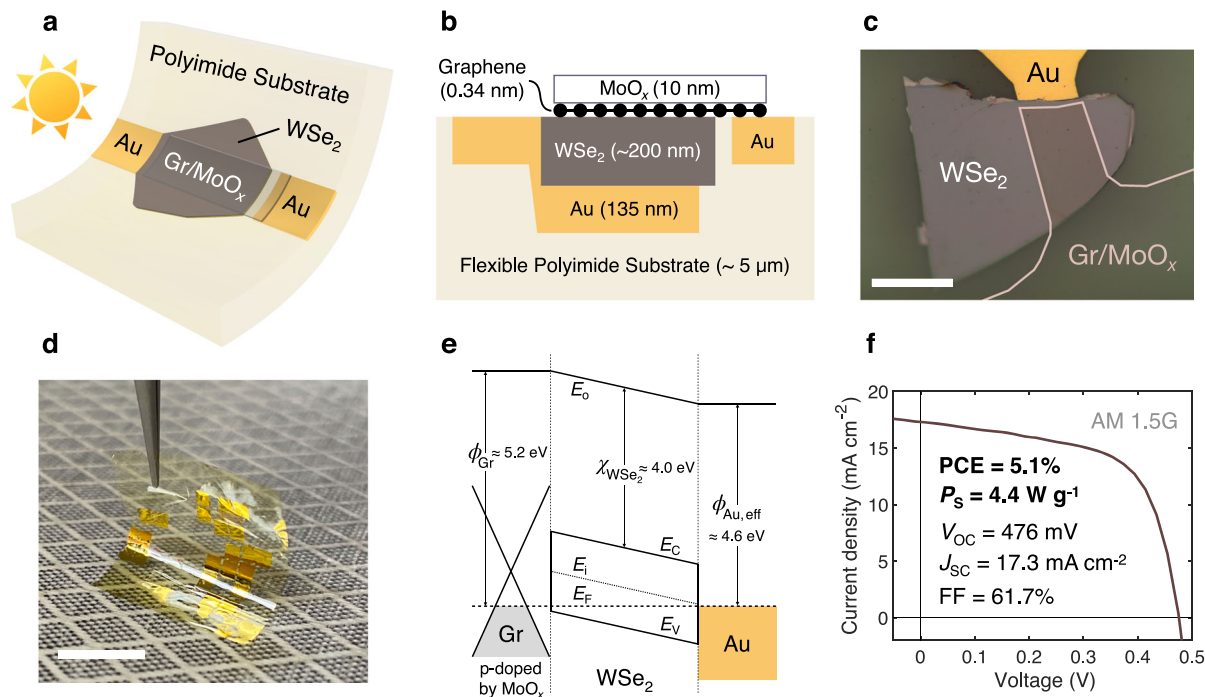
**Fig. 1 Flexible WSe$_2$ solar cells. a** Device schematic and **b** cross-section. **c** Top-down optical image of the device. Scale bar, 50 µm. **d** Photograph of WSe$_2$ solar cells on a flexible polyimide substrate. Scale bar, 1 cm. **e** Qualitative energy band diagram of the device. The Fermi level ($E_F$) is pinned near the midgap at the Au–WSe$_2$ interface, but not at the van der Waals graphene (Gr)–WSe$_2$ interface[26,32,33,50,51]. MoO$_x$ increases the Gr work function and the built-in potential of the Gr–WSe$_2$ Schottky junction[53]. $E_O$, vacuum level; $E_C$, conduction band edge; $E_V$, valence band edge; $E_i$, intrinsic Fermi level; $\Phi_{Au, eff}$, Au effective work function; $\Phi_{Gr}$, Gr work function; $\chi_{WSe_2}$, electron affinity of WSe$_2$. **f** Measured current density $J$ vs. voltage $V$ under AM 1.5 G illumination. PCE, power conversion efficiency. $P_S$ specific power or power per weight. $V_{OC}$ open-circuit voltage. $J_{SC}$ short-circuit current. FF fill factor.

**Photovoltaic performance.** Under global air mass AM 1.5 G illumination, the flexible WSe$_2$ solar cells achieve $V_{OC}$ of 476 mV, a $J_{SC}$ of 17.3 mA cm$^{-2}$, and a fill factor (FF) of 61.7% (Fig. 1f), leading to an unprecedented PCE of 5.1% in flexible TMD solar cells, over 10× higher than previous demonstrations (<0.7%)[20]. Having an ultrathin absorber layer and a lightweight polyimide substrate, these WSe$_2$ solar cells also achieve a high-specific power ($P_S$) of 4.4 W g$^{-1}$ (calculated in Supplementary Note 3 using the data in Supplementary Table 2), over 100× higher than preceding results (<0.04 W g$^{-1}$)[20] and on par with champion solar cells from well-established thin-film technologies CdTe, CIGS, a-Si, and III-Vs[38–45]. The device has a shunt resistance of 226 Ω cm$^2$ and a series resistance of 3.1 Ω cm$^2$, calculated by inversing the slope of the $J-V$ curve at short-circuit and open-circuit conditions, respectively, yielding the reasonable FF of 61.7%. We measure reproducible performance in all nine devices fabricated (Supplementary Fig. 4). No hysteresis is observed in the $J-V$ characteristics when sweeping the voltage in the forward and backward directions (Supplementary Fig. 5). Similar $J-V$ characteristics are observed in solar cells with undoped tungsten disulfide (WS$_2$) absorber layers. However, due to their lower built-in potential, WS$_2$ solar cells exhibit lower $V_{OC}$, $J_{SC}$, FF, and hence PCE (Supplementary Fig. 6).

**Electrical characterization.** Next, we measure the current density vs. voltage ($J-V$) characteristics of flexible WSe$_2$ solar cells in the dark and for AM 1.5 G illumination at various incident power intensities (Fig. 2a, b). As shown in Fig. 1e, Au is not an ohmic n-type contact and, similar to Gr, forms a Schottky junction with WSe$_2$, resulting in a back-to-back diode structure (Fig. 2a, inset). This undesirable Schottky barrier at the Au back contact leads to the roll-over phenomenon where the slope of the $J-V$ curve is reduced at high forward biases[57,58], starting here at around

$V = 0.65$ V. The barrier also causes the cross-over of dark and light $J-V$ curves at $V = 0.53$ V, which can be explained by the presence of a minority carrier surface recombination current at the Au–WSe$_2$ interface[58]. The two phenomena are also frequently observed in CdTe and CIGS solar cells[57–59].

Figure 2b shows a zoomed-in view of the photovoltaic region. An analysis of this data indicates that the shunt resistance decreases almost linearly with increasing incident intensity (Supplementary Fig. 7). This phenomenon, known as photo-shunting, occurs due to increased minority carrier conductivity across the device under illumination[60,61]. Improving the charge carrier selectivity of the solar cell, for example by utilizing carrier-selective metal-interlayer-semiconductor (MIS) contacts or introducing a high built-in potential p–n homojunction could reduce or eliminate photoshunting. Given the initially high shunt resistance of the device, photoshunting does not affect the shape of the $J-V$ curve, and therefore fill factor stays constant at various intensities.

By fitting a power-law equation on the measured current density and incident power data (Fig. 2c), we observe that short-circuit current density versus incident power follow a linear trend ($J_{SC} = \beta \cdot (P_{in})^\alpha$, $\alpha = 1$), expected from a well-designed solar cell. Equation 1 is a rearrangement of the diode equation in the presence of photogeneration ($J_{photo} = J_{SC}$) and shunt resistance ($R_{SH}$) at $V = V_{OC}$, leading to zero current density by definition ($J = 0$). In this equation, $n$ is the diode ideality factor, $k_B$ is the Boltzmann constant, $T$ is the absolute temperature, $q$ is the elementary charge, and $J_o$ is the dark saturation current. According to this equation, $V_{OC}$ scales linearly with $\ln(J_{SC} - V_{OC}/R_{SH})$ when $(J_{SC} - V_{OC}/R_{SH})/J_o \gg 1$, valid for the WSe$_2$ solar cells in this study. By fitting the measured $V_{OC}$ and $J_{SC} - V_{OC}/R_{SH}$ (Fig. 2d), we extract $n$ and $J_o$ of the WSe$_2$ solar cells, neglecting the Au back Schottky diode for simplicity.
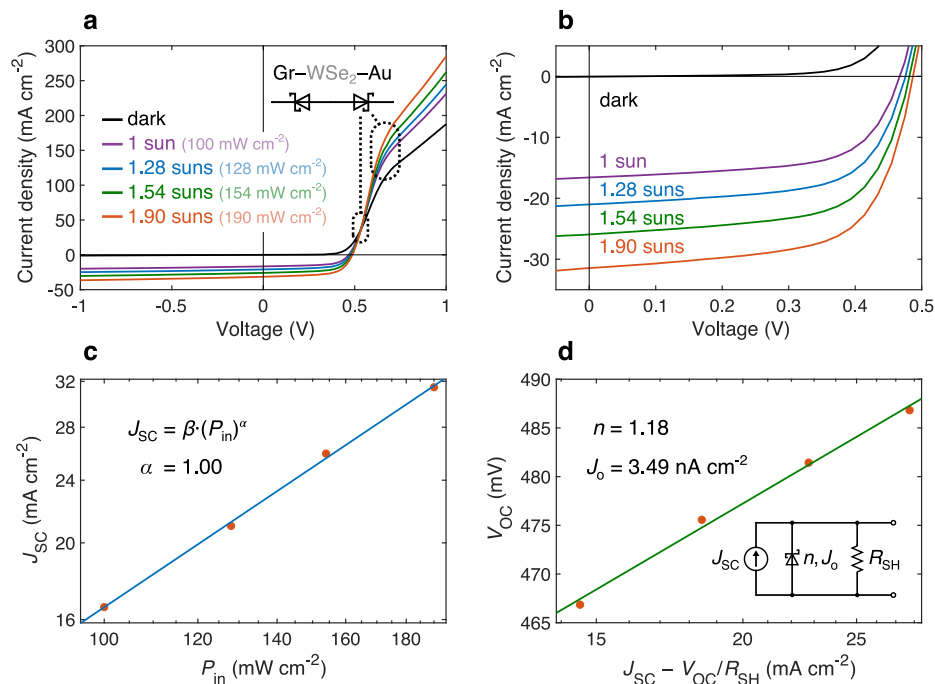
**Fig. 2 Electrical characteristics of flexible WSe$_2$ solar cells. a** Current density vs. voltage (J-V) characteristics of WSe$_2$ solar cells under AM 1.5 G illumination, at various incident power. Inset represents the circuit diagram of Au–WSe$_2$ and Gr–WSe$_2$ junctions. With its Fermi level pinned around midgap, Au forms a Schottky junction to WSe$_2$ opposing the main Gr–WSe$_2$ Schottky junction, leading to cross-over and roll-over effects occurring around 0.53 and 0.65 V, respectively[57,58], as marked by dotted ovals. **b** Zoomed-in view of the photovoltaic region of the J-V measurements shown in **a**. **c** Short-circuit current density (J$_{SC}$) of the devices. P$_{in}$, incident power; symbols, measurements; line, power law fit. **d** Open-circuit voltage (V$_{OC}$) of the devices. Note logarithmic axes in **c** and horizontal axis in **d**. R$_{SH}$, shunt resistance; symbols, measurements; line, fit. Inset shows a representative circuit diagram. n is the ideality factor and J$_o$ the dark saturation current density from the diode fit.

WSe$_2$ solar cells demonstrate a desirable near-unity ideality factor of $n = 1.18$ and dark saturation current of $J_o = 3.49\,\text{nA cm}^{-2}$. The near-unity ideality factor and small dark saturation current indicate low levels of charge carrier recombination and therefore a high internal quantum efficiency as confirmed later by comparing the measured $J_{SC}$ and $J_{SC,\,max}$ derived from absorption measurements.

$$V_{OC} = \frac{nk_BT}{q}\ln\left(\frac{J_{SC} - \frac{V_{OC}}{R_{SH}}}{J_o} + 1\right) \qquad (1)$$

**Optical characterization and simulation.** Figure 3a shows the optical image, spatial light beam-induced current (LBIC or photocurrent) map acquired at a wavelength of 530 nm, and their overlay for a typical flexible WSe$_2$ solar cell. The overlay map shows that only the Gr–WSe$_2$ diode is responsible for splitting photogenerated holes and electrons and therefore producing photocurrent. No photocurrent generation is observed at the Au–WSe$_2$ back diode. This can be seen at the narrow WSe$_2$ region near the Au contact line on the left, where the Au bottom contact is present, but no Gr is covering the WSe$_2$. In contrast, a strong photocurrent is measured on the opposite side of the WSe$_2$ on the right, where the Au back contact is absent and WSe$_2$ is only in contact with Gr. This is further visualized by a cross-shaped contact scheme in Supplementary Fig. 8.

To accurately define the active area of the device, the photocurrent profile across the width of the device (x axis in Fig. 3a) is plotted on a linear scale (Fig. 3b). In this specific device, MoO$_x$ is slightly misaligned with respect to Gr (Fig. 3a). The misalignment only occurred in few devices due to lithography issues. Most devices, such as the one shown in Fig. 1f, have well-aligned Gr and MoO$_x$. On the left edge of Fig. 3b (corresponds to the upper edge in the photocurrent map), photocurrent is only generated in regions covered by Gr. The tail beyond the Gr edge occurs due to the finite laser spot size (~2 μm), leading to spatial averaging of the photocurrent. This spatial averaging shows up as a ~2-μm tail going from non-zero to zero photocurrent regimes as visible in the photocurrent profile. On the right side of Fig. 3b (corresponds to the lower edge in the photocurrent map), due to the passivation effect of MoO$_x$[24], current generation goes beyond Gr and occurs up to the MoO$_x$ right edge. A similar spatial averaging phenomenon is also taking place on this side, resulting in a ~2-μm tail beyond the MoO$_x$ edge. The photocurrent profile confirms that photogeneration only occurs in regions covered by Gr (and MoO$_x$, if misaligned) and this area can be used to accurately define the active area of the device for current density calculation, similar to other studies on vertical TMD solar cells[22]. The active area of the solar cells tested varies from ~$10^3$ to ~$10^4$ μm$^2$.

We measure the absorption spectrum of WSe$_2$ solar cells at different stages of fabrication, i.e., after polyimide release (Au–WSe$_2$), after Gr transfer (Au–WSe$_2$–Gr), and finally after MoO$_x$ deposition (Au–WSe$_2$–Gr–MoO$_x$), as shown in Fig. 3c. For consistency, each measurement is taken at exactly the same spot at the center of the active area of the device. The data in Fig. 3c corresponds to the device whose J-V characteristics are shown in Fig. 1f. This device has a 209-nm-thick WSe$_2$ absorber layer, as measured by a stylus-based surface profiler.

After transferring Gr on top of WSe$_2$, the overall absorption of the stack is slightly reduced. Optical simulations using the transfer matrix method produce a similar result (Supplementary Fig. 9a). Depositing 10 nm of MoO$_x$ on top of Gr increases the
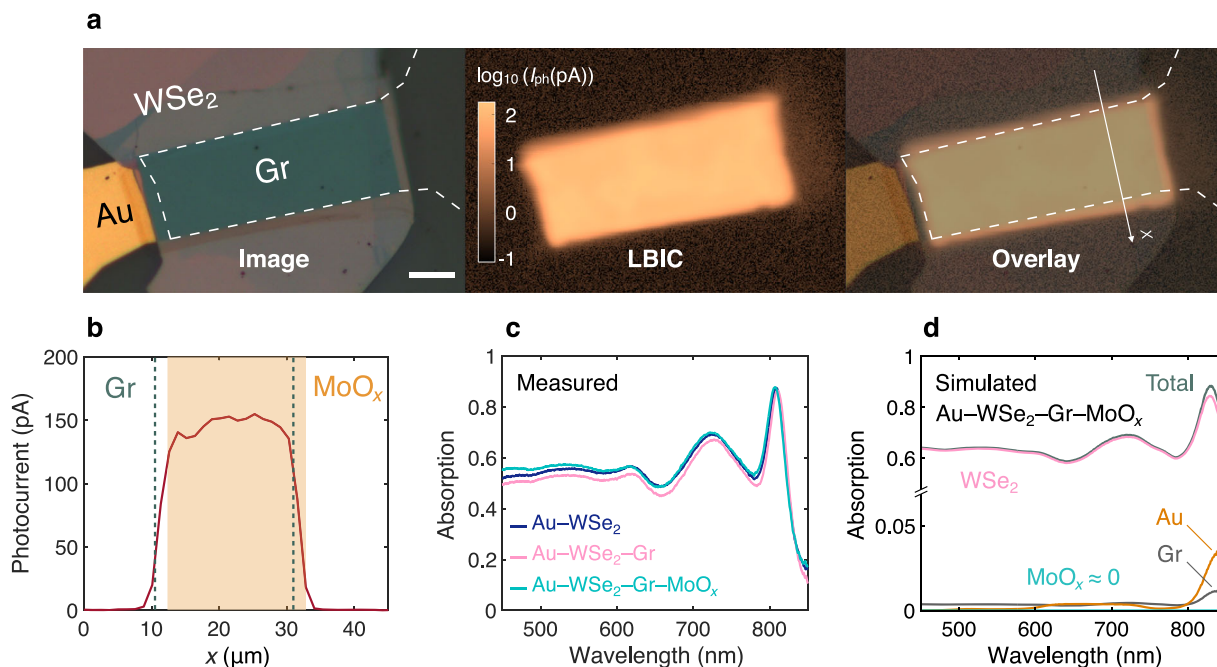
**Fig. 3 Optical characteristics of flexible WSe₂ solar cells. a** Optical image (left), light beam-induced current (LBIC or photocurrent) map (middle), and their overlay (right) for a typical WSe₂ solar cell, measured at $\lambda = 530$ nm. Scale bar, 10 μm. **b** Photocurrent profile along the x axis shown in **a**, demonstrating that the Gr/MoO$_x$–WSe₂ junction area accurately represents the active area of the solar cell. The misaligned MoO$_x$ is passivating the WSe₂ top surface[24], leading to the current generation up to the edge of MoO$_x$. The photocurrent tails beyond the edges of Gr and MoO$_x$ occur due to the finite laser spot size (~2 μm). In most devices, MoO$_x$ and Gr are fully aligned like in Fig. 1c. **c** Measured absorption spectra at the center of the active area, taken at various stages of the fabrication process: after polyimide release (only with Au–WSe₂), Gr transfer, and MoO$_x$ deposition. **d** Simulated absorption spectra of the same device, matching well with the measurement in **c**. The plot also shows the contribution of each layer to the overall absorption. Nearly all absorption occurs within the 209-nm-thick WSe₂ absorber layer. Note the discontinuous vertical axis, used to magnify the smaller contributions.
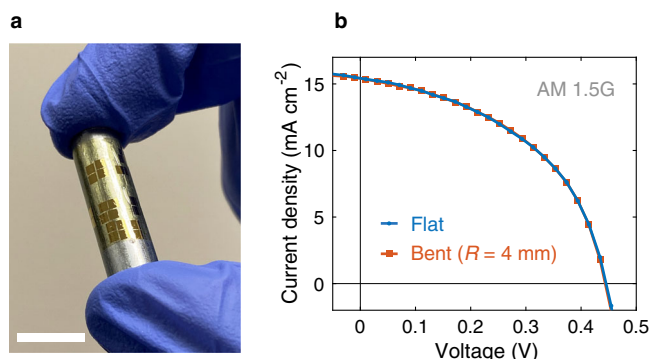


**Fig. 4 Bending test. a** Photograph of the bending setup. The polyimide substrate is attached to an 8-mm-diameter metal cylinder, causing bending of the substrate at a curvature radius of 4 mm. Scale bar, 1 cm. **b** Measured J–V characteristics of a typical flexible WSe₂ solar cell under AM 1.5 G illumination in flat and bent conditions. Bending does not change the J–V characteristics of the device.

overall absorption of the stack. This can be either due to parasitic absorption within MoO$_x$ or its anti-reflection coating effect improving the absorption within the WSe₂ absorber layer. To answer this question, we simulate absorption using the transfer matrix method. Figure 3d shows a simulated absorption spectrum of the Au–WSe₂–Gr–MoO$_x$ stack along with the contribution of each individual layer. Simulated and measured absorption spectra are in good agreement, having the same shapes and magnitudes, with peaks and valleys located at similar wavelengths. The small discrepancies between the two absorption spectra can be

explained by the fact that the optical properties of WSe₂ used in the simulation are taken from the literature[62] and may deviate slightly from the WSe₂ films in this study.

According to Fig. 3d, parasitic absorption in the 10-nm MoO$_x$ layer is essentially zero. In addition, nearly all absorption occurs within the 209-nm-thick WSe₂ absorber layer, indicating that the absorption boost observed after MoO$_x$ coating (Fig. 3c) is mainly due to the increased absorption in the WSe₂ layer. These observations suggest that MoO$_x$ is acting as an anti-reflection coating for the WSe₂ absorber layer. Our optical simulation confirms this hypothesis (Supplementary Fig. 9b, c), showing that adding MoO$_x$ increases the absorption within the WSe₂ layer. The simulation also reveals that an optimal choice of MoO$_x$ thickness (~70 nm) can lead to a significant improvement in $J_{SC}$ values up to 30 mA cm$^{-2}$ (Supplementary Fig. 9c, d). This suggests that MoO$_x$ could be used as a simple yet effective anti-reflection coating choice for TMD photovoltaics, to be further investigated in future studies.

The WSe₂ solar cells show an average optical absorption of about 55% over the 450–850 nm wavelength spectrum. Using the simulated WSe₂ absorption spectrum and assuming unity internal quantum efficiency (IQE), we calculate a maximum $J_{SC}$ of 20.0 mA cm$^{-2}$, slightly underestimated because absorption at wavelengths below 400 nm and above 1000 nm are excluded due to lack of available material data (see Supplementary Fig. 9d). Given the measured $J_{SC}$ of 17.3 mA cm$^{-2}$ (Fig. 1f), this implies an average IQE (weighted by AM 1.5 G spectrum) of 0.87, which signals low levels of charge carrier recombination, in agreement with near-unity ideality factor and small dark saturation current extracted from J–V measurements (Fig. 2d). Similar IQE values have been observed in other vertical Schottky junction TMD solar cells[22].

**Bending test**. To test the performance of devices under bending, we attach the polyimide substrate onto an 8-mm-diameter metal cylinder, which bends the substrate at a curvature radius of 4 mm (Fig. 4a). The flexible $WSe_2$ solar cells show the same $J$–$V$ characteristics in flat and bent states under AM 1.5 G illumination (Fig. 4b), indicating consistent performance levels under bending. This is not surprising because given the polyimide substrate thickness of only 5 μm, the materials encounter small strain values of ~0.06% at this bending radius[46], and we expect that sub-millimeter bending radii should be possible given that materials involved have been shown to sustain strains of at least 0.5%[63–68]. We have investigated similar TMD, metal, and dielectric stacks in electronic devices in more detail in our recent work and found that there is no discernable change of electrical device properties[46]. Scaling up the solar cell area will not change the device stability under strain[63,69], however, we expect effects of substrate curvature on light-coupling to become relevant. For instance, it has been found that $J_{SC}$ and PCE reduce[70–72] by ~30% under an incident angle of 45°. With the bending radius of 4 mm, this would mean that a ~6.3 mm wide solar cell would encounter such a 30% reduction at its outermost edges. Hence, for our solar cells with small, exfoliated flakes on length scales that are tens of microns, there is no effect of substrate curvature on the light-coupling, as seen in Fig. 4b. In the future, if the active area of the solar cell is increased, e.g., by large-area synthesis of TMDs, these bending studies will become more important to quantify the effects of the bent surface on light-coupling and thus $J_{SC}$, which would alter solar cell performance.

**Benchmarking and projections**. Figure 5 benchmarks the PCE and $P_S$ of the flexible $WSe_2$ solar cells in this work against other thin-film solar technologies (details in Supplementary Note 4). The flexible $WSe_2$ solar cells in this study demonstrate remarkable improvements of about 10× and 100× in PCE and $P_S$,

respectively, compared to the previous results in flexible TMD solar cells (PCE < 0.7% and $P_S$ < 0.04 W g$^{-1}$)[20]. With only a moderate PCE of 5.1%, the $WSe_2$ solar cells already achieve a high-specific power of 4.4 W g$^{-1}$ enabled by their ultrathin $WSe_2$ absorber layer and lightweight polyimide substrate. This high $P_S$ is in the same range as champion solar cells of well-established thin-film technologies CdTe (II-VI), CIGS, a-Si, and III-Vs[38–45].

By reducing the polyimide substrate thickness to 1 μm, same as in some of the champion organic PV (OPV) and perovskite solar cells in Fig. 5, specific power can be further increased to 8.6 W g$^{-1}$ (path #1 in Fig. 5). According to realistic detailed balance models developed for TMD photovoltaic cells, single-junction multilayer TMDs can in principle achieve ~27% PCE with an optimized optical and electronic design[13]. We have estimated similar values specifically for $WSe_2$ solar cells as shown in Supplementary Note 5 and Supplementary Fig. 10. Such PCE would lead to an ultrahigh specific power of 46 W g$^{-1}$ (path #2 in Fig. 5), by far outperforming all other thin-film technologies, including perovskite solar cells which currently hold the record for specific power (29.4 W g$^{-1}$)[73]. In addition, TMD solar cells do not have the stability challenges of OPV or perovskites, and in contrast to high-performing perovskites and lead sulfide (PbS) quantum dots, they do not contain toxic elements such as lead, and therefore are not expected to pose any significant environmental or health hazards[74].

**Future research**. In order to achieve the projected ~27% PCE in the flexible $WSe_2$ solar cells, both optical and electronic designs need to be improved. As pointed out earlier, $MoO_x$ can serve as an effective anti-reflection coating for $WSe_2$. Our optical simulation shows that simply increasing the thickness of $MoO_x$ to an optimal value of ~70 nm is supposed to improve the absorption within the $WSe_2$ layer to 80% and enable $J_{SC}$ values up to 30 mA cm$^{-2}$ (Supplementary Fig. 9c, d). Metasurface-based plasmonic light-trapping schemes can help further improve absorption and reach $J_{SC}$ values near the Shockley–Queisser limit (40 mA cm$^{-2}$ for a bandgap of 1.2 eV)[75–79].

$V_{OC}$ is another important area of improvement. The built-in potential and therefore $V_{OC}$ of these devices can be improved by employing n-type $WSe_2$. The doping process can be performed during growth, or by means of ultrathin metal-oxide interlayers such as $AlO_x$ and $TiO_x$ placed between the TMD absorber layer and the metallic bottom contact[80,81]. Replacing Au with a lower work function metal but ensuring a similar interface quality could also improve $V_{OC}$. We showed in our experiments that Al and Ti are not good candidates for this purpose (Supplementary Fig. 2). Forming a high built-in potential p–n heterojunction (e.g., $WSe_2$/$MoS_2$) or homojunction, possibly by metal-oxide-based p-type ($MoO_x$) and n-type ($AlO_x$) doping, is another way to achieve a high $V_{OC}$[23–25,80,82,83]. One can also improve the $V_{OC}$ by adopting carrier-selective (MIS) contacts which both de-pin the Fermi level and enable a selective collection of only one type of charge carrier on each side of the solar cell[28–31,84,85].

Research efforts to scale up TMD growth to large areas would soon enable scalable and low-cost production of TMD photovoltaic cells[86,87], similar to other chalcogenide solar cells CdTe and CIGS. The potential of TMDs to achieve high power conversion efficiency and specific power at a low cost as well as their stability and environmental friendliness (in contrast to perovskites) makes them a serious candidate for next-generation photovoltaics, especially in high-specific-power applications.

In summary, we demonstrated flexible $WSe_2$ solar cells with record-breaking power conversion efficiency PCE of 5.1% and power per weight $P_S$ of 4.4 W g$^{-1}$. We performed detailed optical and electrical characterizations on these solar cells to explain their
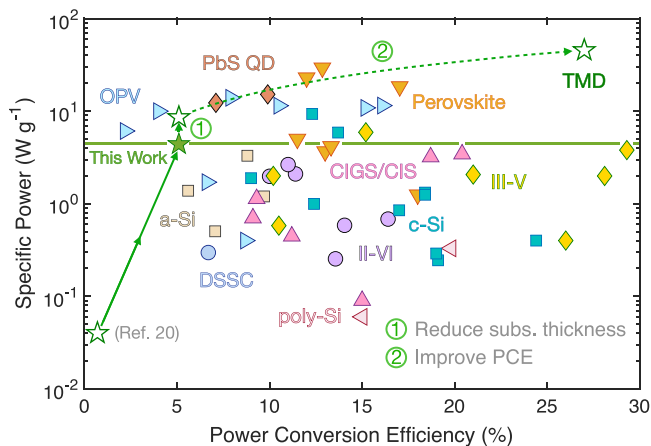


**Fig. 5 Power conversion efficiency (PCE) and specific power (power per weight) of lightweight and flexible thin-film solar technologies.** Our flexible TMD ($WSe_2$) solar cell achieves a relatively high specific power despite its moderate PCE (filled green star). Arrow 1 shows the projected effect of reducing substrate thickness, arrow 2 shows the projected effect of improving PCE. With these improvements, TMD solar cells could reach unprecedented specific power in the future. More details are given in Supplementary Note 4. OPV organic photovoltaics, PbS QD lead sulfide quantum dot, CIGS/CIS copper indium (gallium) selenide, c-Si crystalline silicon, a-Si amorphous silicon, poly-Si polycrystalline silicon, DSSC dye-sensitized solar cell, III-V (II-VI) compound semiconductors containing elements from groups three and five (or two and six) in the periodic table (see Supplementary Table 3 for more details and references).

superior performance and identify areas of improvement, providing practical guidelines on the optical and electronic design to enhance PCE and $P_S$. We also tested the flexible solar cells under bending and showed similar performance in flat and bent states. Future large-area TMD cells will require more bending studies to verify the effects of light-coupling at different angles on solar cell performance. Lastly, we benchmarked the flexible WSe$_2$ solar cells against other thin-film photovoltaic technologies and showed their potential to achieve ultrahigh $P_S$, creating unprecedented opportunities in a broad range of industries from aerospace to wearable electronics.

## Methods

**Device fabrication**. The details on device fabrication are provided in Supplementary Note 1. In short, WSe$_2$ flakes were mechanically exfoliated onto Si/SiO$_2$ substrates. Next, 135 nm of Au serving as solar cell bottom contacts was electron-beam evaporated and structured by optical photolithography and lift-off. Then the flexible polyimide substrate was spin-coated on top, cured and all structures were released together in deionized water. After flipping the substrate, graphene was wet-transferred as transparent top contact and structured by optical photo-lithography and dry etching. Finally, MoO$_x$ was deposited by electron-beam eva-poration and structured by optical photolithography and lift-off, followed by annealing in ambient air for the purpose of doping, passivation, and anti-reflection coating. The process flow is schematically shown in Supplementary Fig. 1. The thickness of WSe$_2$ flakes was measured by atomic force microscopy (AFM, Bruker Dimension Icon) and/or stylus-based surface profilometry (Alphastep 500) after exfoliation on the Si/SiO$_2$ substrate.

**AM 1.5 G current–voltage measurements**. AM 1.5 G I–V measurements were done using a digital source meter (Keithley 2420) and a class AAA solar simulator (Newport, Oriel Sol3A Class AAA) having a 450 W xenon short arc lamp and AM 1.5 G spectral correction filter. Lamp intensity calibration was done using a silicon reference cell (Newport, Oriel 91150 V) placed at the location of the sample. The silicon reference cell was calibrated by Newport Corporation. I–V characteristics were measured with a scan rate of 200 mV s$^{-1}$ and a dwell time of 30 ms. The measurements were performed in air. The samples were kept at room temperature via convection cooling provided by a fan. In all I–V measurements, the voltage was applied to the graphene top contact, while the gold bottom contact was grounded.

**Photocurrent mapping**. The photocurrent from the device was measured on a custom-built optoelectronic setup. A supercontinuum laser source (Fianium) and an acousto-optic tunable filter (Fianium) were used to provide monochromatic illumination across a broad spectral range. To achieve a high signal-to-noise ratio, the laser light was modulated by a chopper wheel (400 Hz) synchronized with two lock-in amplifiers. The laser light was focused onto the sample using a 50X long working distance objective (Mitutoyo M Plan APO NIR). To image the sample, two beam splitters were placed in the illumination path for a halogen lamp and a charge-coupled device (CCD) imaging camera, respectively. Using a glass slide, a small fraction of the reflected light was directed into a large-area Si photodiode (New Focus, model 2031) connected to a lock-in amplifier (Stanford Research SR810 DSP) to measure reflection from the sample. The sample was placed on a chip carrier and then mounted on a three-axis piezo stage to accurately control its spatial position. Electrical connections were made by soldering wires (34-gauge enameled wires) using thermally stable solder paste Sn42/Bi57.6/Ag0.4 T4 (Chip Quik) onto the Au metal pads. To measure the photocurrent, the mounted sample was connected in series with a source meter (Keithley 2612), a tunable current-to-voltage amplifier, and a second lock-in amplifier (Stanford Research SR810 DSP).

**Absorption measurement**. The absorption measurements were performed using a Nikon C2 confocal microscope coupled to a CCD camera (Acton Pixis 1024, Princeton Instrument) and a spectrometer (Acton SP2300i, Princeton Instrument). Unpolarized light from a halogen lamp was used to illuminate the sample through a 20X objective (Nikon CFI Achromat LWD, NA = 0.4). The reflection spectra ($R(\lambda)$) were normalized to the calibrated reflection spectrum of a protected silver mirror (Thorlabs, PF10-03-P01). Since all devices were fabricated on top of thick Au contact, the absorption spectra ($A(\lambda)$) were calculated by $A(\lambda) = 1 - R(\lambda)$.

**Raman spectroscopy**. The Raman measurements were performed on a HORIBA Scientific LabRAM HR Evolution spectrometer using an excitation wavelength of 532 nm. For Raman measurements, an acquisition time, accumulations, laser power, and the optical grating of 20 s, 2, 2.8 mW, 1800 gr mm$^{-1}$ were used, and the spot size is <1 μm.

**Optical simulation**. Optical simulations were performed using the transfer matrix method. A normally incident plane wave was assumed in all simulations. The thickness of each layer used in simulations is shown in Fig. 1b. The bottom Au

contact was modeled as a semi-infinite substrate due to its small penetration depth. Optical constants for WSe$_2$, Gr, and Au were taken from the literature[62,88,89]. Optical constants for MoO$_x$ were obtained experimentally from spectroscopic ellipsometry ($n \approx 2.0$).

## Data availability
The data that support the findings of this study are available from the corresponding author upon reasonable request.

## References
1. Philipps, S. et al. *Photovoltaics Report* (Fraunhofer Institute for Solar Energy Systems, 2020).
2. Jeong, S., McGehee, M. D. & Cui, Y. All-back-contact ultra-thin silicon nanocone solar cells with 13.7% power conversion efficiency. *Nat. Commun.* **4**, 2950 (2013).
3. Lee, S.-M. et al. Printable nanostructured silicon solar cells for high-performance, large-area flexible photovoltaics. *ACS Nano* **8**, 10507–10516 (2014).
4. Lin, Q. et al. High performance thin film solar cells on plastic substrates with nanostructure-enhanced flexibility. *Nano Energy* **22**, 539–547 (2016).
5. Sun, X. et al. Firmly standing three-dimensional radial junctions on soft aluminum foils enable extremely low cost flexible thin film solar cells with very high power-to-weight performance. *Nano Energy* **53**, 83–90 (2018).
6. Das, S. et al. A leaf-inspired photon management scheme using optically tuned bilayer nanoparticles for ultra-thin and highly efficient photovoltaic devices. *Nano Energy* **58**, 47–56 (2019).
7. Xue, M. et al. Free-standing 2.7 μm thick ultrathin crystalline silicon solar cell with efficiency above 12.0%. *Nano Energy* **70**, 104466 (2020).
8. Kaltenbrunner, M. et al. Flexible high power-per-weight perovskite solar cells with chromium oxide–metal contacts for improved stability in air. *Nat. Mater.* **14**, 1032–1039 (2015).
9. Reese, M. O. et al. Increasing markets and decreasing package weight for high-specific-power photovoltaics. *Nat. Energy* **3**, 1002–1012 (2018).
10. Song, Y., Min, J. & Gao, W. Wearable and implantable electronics: moving toward precision therapy. *ACS Nano* **13**, 12280–12286 (2019).
11. Mak, K. F., Lee, C., Hone, J., Shan, J. & Heinz, T. F. Atomically thin MoS$_2$: a new direct-gap semiconductor. *Phys. Rev. Lett.* **105**, 2–5 (2010).
12. Splendiani, A. et al. Emerging photoluminescence in monolayer MoS$_2$. *Nano Lett.* **10**, 1271–1275 (2010).
13. Jariwala, D., Davoyan, A. R., Wong, J. & Atwater, H. A. Van der Waals materials for atomically-thin photovoltaics: promise and outlook. *ACS Photonics* **4**, 2962–2970 (2017).
14. Bernardi, M., Palummo, M. & Grossman, J. C. Extraordinary sunlight absorption and one nanometer thick photovoltaics using two-dimensional monolayer materials. *Nano Lett.* **13**, 3664–3670 (2013).
15. Jariwala, D. et al. Near-unity absorption in van der Waals semiconductors for ultrathin optoelectronics. *Nano Lett.* **16**, 5482–5487 (2016).
16. Huang, L. et al. Atomically thin MoS$_2$ narrowband and broadband light superabsorbers. *ACS Nano* **10**, 7493–7499 (2016).
17. Wang, L. et al. 2D photovoltaic devices: progress and prospects. *Small Methods* **1700294**, 1700294 (2018).
18. Wang, H. et al. Two-dimensional heterostructures: fabrication, characterization, and application. *Nanoscale* **6**, 12250–12272 (2014).
19. Li, H.-M. et al. Ultimate thin vertical p–n junction composed of two-dimensional layered molybdenum disulfide. *Nat. Commun.* **6**, 6564 (2015).
20. Akama, T. et al. Schottky solar cell using few-layered transition metal dichalcogenides toward large-scale fabrication of semitransparent and flexible power generator. *Sci. Rep.* **7**, 11967 (2017).
21. Mao, X., Zou, J., Li, H., Song, Z. & He, S. Magnetron sputtering fabrication and photoelectric properties of WSe$_2$ film solar cell device. *Appl. Surf. Sci.* **444**, 126–132 (2018).
22. Went, C. M. et al. A new metal transfer process for van der Waals contacts to vertical Schottky-junction transition metal dichalcogenide photovoltaics. *Sci. Adv.* **5**, eaax6061 (2019).
23. McVay, E., Zubair, A., Lin, Y., Nourbakhsh, A. & Palacios, T. Impact of Al$_2$O$_3$ passivation on the photovoltaic performance of vertical WSe$_2$ Schottky junction solar cells. *ACS Appl. Mater. Interfaces* **12**, 57987–57995 (2020).
24. Nassiri Nazif, K. et al. High-performance p–n junction transition metal dichalcogenide photovoltaic cells enabled by MoO$_x$ doping and passivation. *Nano Lett.* **21**, 3443–3450 (2021).

25. Nassiri Nazif, K., Kumar, A., Moreira De Menezes, M. T. & Saraswat, K. Towards high $V_{oc}$, thin film, homojunction $WS_2$ solar cells for energy harvesting applications. *Proc. SPIE, Wide Bandgap Materials, Devices, and Applications IV* **11126**, 7 (2019).

26. Liu, Y. et al. Approaching the Schottky–Mott limit in van der Waals metal–semiconductor junctions. *Nature* **557**, 696–700 (2018).

27. Zhao, Y. et al. Doping, contact and interface engineering of two-dimensional layered transition metal dichalcogenides transistors. *Adv. Funct. Mater.* **27**, 1603484 (2017).

28. Chen, J.-R. et al. Control of Schottky barriers in single layer $MoS_2$ transistors with ferromagnetic contacts. *Nano Lett.* **13**, 3106–3110 (2013).

29. Lee, S., Tang, A., Aloni, S. & Wong, H.-S.P. Statistical study on the Schottky barrier reduction of tunneling contacts to CVD synthesized $MoS_2$. *Nano Lett.* **16**, 276–281 (2015).

30. Mleczko, M.J. et al. Contact Engineering High-Performance n-Type $MoTe_2$ Transistors. *Nano Lett.* **19**, 6352–6362 (2019).

31. Lim, J. et al. Contact engineering of vertically grown $ReS_2$ with Schottky barrier modulation. *ACS Appl. Mater. Interfaces* **13**, 7529–7538 (2021).

32. Le Quang, T. et al. Scanning tunneling spectroscopy of van der Waals graphene/semiconductor interfaces: absence of Fermi level pinning. *2D Mater.* **4**, 35019 (2017).

33. LaGasse, S. W., Dhakras, P., Watanabe, K., Taniguchi, T. & Lee, J. U. Gate-tunable graphene–$WSe_2$ heterojunctions at the Schottky–Mott limit. *Adv. Mater.* **31**, 1901392 (2019).

34. Yeh, C.-H. et al. Graphene–transition metal dichalcogenide heterojunctions for scalable and low-power complementary integrated circuits. *ACS Nano* **14**, 985–992 (2020).

35. Wi, S. et al. Enhancement of photovoltaic response in multilayer $MoS_2$ induced by plasma doping. *ACS Nano* **8**, 5270–5281 (2014).

36. Memaran, S. et al. Pronounced photovoltaic response from multilayered transition-metal dichalcogenides PN-junctions. *Nano Lett.* **15**, 7532–7538 (2015).

37. Shinde, S. M. et al. Surface-functionalization-mediated direct transfer of molybdenum disulfide for large-area flexible devices. *Adv. Funct. Mater.* **28**, 1706231 (2018).

38. Romeo, A., Arnold, M., Bätzner, D. L., Zogg, H. & Tiwari, A. N. Development of high efficiency flexible solar cells. *PV Eur. PV Technol. Energy Solut.* **1**, 377–381 (2002).

39. Romeo, A. et al. High-efficiency flexible CdTe solar cells on polymer substrates. *Sol. Energy Mater. Sol. Cells* **90**, 3407–3415 (2006).

40. Chirilă, A. et al. Highly efficient Cu(In,Ga)Se$_2$ solar cells grown on flexible polymer films. *Nat. Mater.* **10**, 857–861 (2011).

41. Chirilă, A. et al. Potassium-induced surface modification of Cu(In,Ga)Se$_2$ thin films for high-efficiency solar cells. *Nat. Mater.* **12**, 1107–1111 (2013).

42. Söderström, T., Haug, F.-J., Terrazzoni-Daudrix, V. & Ballif, C. Optimization of amorphous silicon thin film solar cells for flexible photovoltaics. *J. Appl. Phys.* **103**, 114509 (2008).

43. Xu, X. et al. High efficiency ultra lightweight a-Si:H/a-SiGe:H/a-SiGe:H triple-junction solar cells on polymer substrate using roll-to-roll technology. In *2008 33rd IEEE Photovoltaic Specialists Conference* 1–6 (2008).

44. Kim, J. et al. Ultra-thin flexible GaAs photovoltaics in vertical forms printed on metal surfaces without interlayer adhesives. *Appl. Phys. Lett.* **108**, 253101 (2016).

45. Cardwell, D. et al. Very high specific power ELO solar cells (>3 kW/kg) for UAV, space, and portable power applications. In *2017 IEEE 44th Photovoltaic Specialist Conference (PVSC)* 3511–3513 (2017).

46. Daus, A. et al. High-performance flexible nanoscale transistors based on transition metal dichalcogenides. *Nat. Electron.* **4**, 495–501 (2021).

47. Kam, K. K. & Parkinson, B. A. Detailed photocurrent spectroscopy of the semiconducting group VIB transition metal dichalcogenides. *J. Phys. Chem.* **86**, 463–467 (1982).

48. Traving, M. et al. Electronic structure of $WSe_2$: a combined photoemission and inverse photoemission study. *Phys. Rev. B* **55**, 10392–10399 (1997).

49. Schlaf, R., Lang, O., Pettenkofer, C. & Jaegermann, W. Band lineup of layered semiconductor heterointerfaces prepared by van der Waals epitaxy: charge transfer correction term for the electron affinity rule. *J. Appl. Phys.* **85**, 2732–2753 (1999).

50. Das, S. & Appenzeller, J. $WSe_2$ field effect transistors with enhanced ambipolar characteristics. *Appl. Phys. Lett.* **103**, 103501 (2013).

51. Lee, I. et al. Non-degenerate n-type doping by hydrazine treatment in metal work function engineered $WSe_2$ field-effect transistor. *Nanotechnology* **26**, 455203 (2015).

52. Schauble, K. et al. Uncovering the effects of metal contacts on monolayer $MoS_2$. *ACS Nano* **14**, 14798–14808 (2020).

53. Vaziri, S. et al. Ultrahigh doping of graphene using flame-deposited $MoO_3$. *IEEE Electron Device Lett.* **41**, 1592–1595 (2020).

54. Yan, R. et al. Determination of graphene work function and graphene-insulator-semiconductor band alignment by internal photoemission spectroscopy. *Appl. Phys. Lett.* **101**, 22105 (2012).

55. Song, S. M., Park, J. K., Sul, O. J. & Cho, B. J. Determination of work function of graphene under a metal electrode and its role in contact resistance. *Nano Lett.* **12**, 3887–3892 (2012).

56. Avsar, A. et al. Reconfigurable diodes based on vertical $WSe_2$ transistors with van der Waals bonded contacts. *Adv. Mater.* **30**, 1707200 (2018).

57. Demtsu, S. H. & Sites, J. R. Effect of back-contact barrier on thin-film CdTe solar cells. *Thin Solid Films* **510**, 320–324 (2006).

58. Niemegeers, A. & Burgelman, M. Effects of the Au/CdTe back contact on IV and CV characteristics of Au/CdTe/CdS/TCO solar cells. *J. Appl. Phys.* **81**, 2881–2886 (1997).

59. Kato, T. et al. Characterization of the back contact of CIGS solar cell as the origin of rollover effect. In *32nd European Photovoltaic Solar Energy Conference and Exhibition* 1085–1088 (2016).

60. Waldauf, C., Scharber, M. C., Schilinsky, P., Hauch, J. A. & Brabec, C. J. Physics of organic bulk heterojunction devices for photovoltaic applications. *J. Appl. Phys.* **99**, 104503 (2006).

61. Würfel, U., Cuevas, A. & Würfel, P. Charge carrier separation in solar cells. *IEEE J. Photovolt.* **5**, 461–469 (2015).

62. Rubio-Bollinger, G. et al. Enhanced visibility of $MoS_2$, $MoSe_2$, $WSe_2$ and black-phosphorus: making optical identification of 2D semiconductors easier. *Electronics* **4**, 847–856 (2015).

63. Senthil Kumar, K., Chen, P.-Y. & Ren, H. A review of printable flexible and stretchable tactile sensors. *Research* **2019**, 3018568 (2019).

64. Münzenrieder, N. et al. Investigation of gate material ductility enables flexible a-IGZO TFTs bendable to a radius of 1.7 mm. In *2013 Proceedings of the European Solid-State Device Research Conference (ESSDERC)* 362–365 (2013).

65. Wang, F. et al. Strain engineering in monolayer $WS_2$ and $WS_2$ nanocomposites. *2D Mater.* **7**, 45022 (2020).

66. Zhang, R., Koutsos, V. & Cheung, R. Elastic properties of suspended multilayer $WSe_2$. *Appl. Phys. Lett.* **108**, 42104 (2016).

67. Abachi, T. et al. Highly flexible, conductive and transparent $MoO_3/Ag/MoO_3$ multilayer electrode for organic photovoltaic cells. *Thin Solid Films* **545**, 438–444 (2013).

68. Lucarelli, G. & Brown, T. M. Development of highly bendable transparent window electrodes based on $MoO_x$, $SnO_2$, and Au dielectric/metal/dielectric stacks: application to indium tin oxide (ITO)-free perovskite solar cells. *Front. Mater.* **6**, 310 (2019).

69. Lewis, J. Material challenge for flexible organic devices. *Mater. Today* **9**, 38–45 (2006).

70. Roy, A. B. et al. Black silicon solar cell: analysis optimization and evolution towards a thinner and flexible future. *Nanotechnology* **27**, 305302 (2016).

71. Roy, A. B., Das, S., Kundu, A., Banerjee, C. & Mukherjee, N. c-Si/n-ZnO-based flexible solar cells with silica nanoparticles as a light trapping metamaterial. *Phys. Chem. Chem. Phys.* **19**, 12838–12844 (2017).

72. Kim, B. J. et al. Highly efficient and bending durable perovskite solar cells: toward a wearable power source. *Energy Environ. Sci.* **8**, 916–921 (2015).

73. Kang, S. et al. Ultrathin, lightweight and flexible perovskite solar cells with an excellent power-per-weight performance. *J. Mater. Chem. A* **7**, 1107–1114 (2019).

74. Fojtů, M., Teo, W. Z. & Pumera, M. Environmental impact and potential health risks of 2D nanomaterials. *Environ. Sci. Nano* **4**, 1617–1633 (2017).

75. Kim, S. J., Fan, P., Kang, J.-H. & Brongersma, M. L. Creating semiconductor metafilms with designer absorption spectra. *Nat. Commun.* **6**, 7591 (2015).

76. Park, J., Kang, J., Kim, S. J., Hasman, E. & Brongersma, M. L. Tuning optical absorption in an ultrathin lossy film by use of a metallic metamaterial mirror. *IEEE Photonics Technol. Lett.* **27**, 1617–1620 (2015).

77. Park, J., Kim, S. J. & Brongersma, M. L. Condition for unity absorption in an ultrathin and highly lossy film in a Gires-Tournois interferometer configuration. *Opt. Lett.* **40**, 1960–1963 (2015).

78. Park, J. et al. Omnidirectional near-unity absorption in an ultrathin planar semiconductor layer on a metal substrate. *ACS Photonics* **1**, 812–821 (2014).

79. Rühle, S. Tabulated values of the Shockley–Queisser limit for single junction solar cells. *Sol. Energy* **130**, 139–147 (2016).

80. McClellan, C. J., Yalon, E., Smithe, K. K. H., Suryavanshi, S. V. & Pop, E. High current density in monolayer $MoS_2$ doped by $AlO_x$. *ACS Nano* **15**, 1587–1596 (2021).

81. Rai, A. et al. Air stable doping and intrinsic mobility enhancement in monolayer molybdenum disulfide by amorphous titanium suboxide encapsulation. *Nano Lett.* **15**, 4329–4336 (2015).

82. Cai, L. et al. Rapid flame synthesis of atomically thin $MoO_3$ down to monolayer thickness for effective hole doping of $WSe_2$. *Nano Lett.* **17**, 3854–3861 (2017).

83. Kumar, A., Nassiri Nazif, K., Ramesh, P. & Saraswat, K. Doped $WS_2$ transistors with large on-off ratio and high on-current. In *2020 Device Research Conference (DRC)* 1–2 (2020).

84. Islam, R., Nassiri Nazif, K. & Saraswat, K. C. Si heterojunction solar cells: a simulation study of the design issues. *IEEE Trans. Electron Devices* **63**, 4788–4795 (2016).

85. Islam, R., Nassiri Nazif, K. & Saraswat, K. Optimization of selective contacts in Si heterojunction photovoltaic cells considering Fermi level pinning and interface passivation. In *IEEE Photovoltaic Specialists Conference* 1–4 (2016).

86. Xiong, L. et al. Research progress on the preparations, characterizations and applications of large scale 2D transition metal dichalcogenides films. *FlatChem* **21**, 100161 (2020).

87. Wang, M. et al. Manufacturing strategies for wafer-scale two-dimensional transition metal dichalcogenide heterolayers. *J. Mater. Res.* **35**, 1350–1368 (2020).

88. Bruna, M. & Borini, S. Optical constants of graphene layers in the visible range. *Appl. Phys. Lett.* **94**, 31901 (2009).

89. Palik, E. D. *Handbook of Optical Constants of Solids* (Academic Press, Cambridge, 1998).

## Acknowledgements

## Author contributions

K.N. and A.D. contributed equally. K.N., A.D., and S.V. conceived the project. K.N. and A.D. fabricated the devices, assisted by S.V., A.K., and M.E.C. J.H. carried out the photocurrent measurements, assisted by S.K. for electrical connections made via soldering. N.L. did the absorption measurements, assisted by J.H. K.N., A.D., and A.K. performed the J–V, Raman/ellipsometry, and AFM measurements, respectively. A.D. and K.N. did the surface profilometry measurements and mechanical bending tests. N.L. and J.H. carried out the optical simulations. F.N. and K.N. performed data analysis on J–V measurements. All authors, i.e., K.N., A.D., J.H., N.L, S.V., A.K., F.N., M.E.C., S.K., R.I., K.-H.K., J.-H.P., A.S.Y.P., M.L.B., E.P., and K.C.S contributed to the data interpretation, presentation, and writing of the manuscript. K.C.S. supervised the work.

## Competing interests

The authors declare no competing interests.

## Additional information

**Supplementary information** The online version contains supplementary material available at https://doi.org/10.1038/s41467-021-27195-7.

**Correspondence** and requests for materials should be addressed to Krishna C. Saraswat.

**Peer review information** *Nature Communications* thanks Kian Loh and the other, anonymous, reviewer(s) for their contribution to the peer review of this work.

**Reprints and permission information** is available at http://www.nature.com/reprints

**Publisher's note** Springer Nature remains neutral with regard to jurisdictional claims in published maps and institutional affiliations.

# Supplementary Information

## High-specific-power flexible transition metal dichalcogenide solar cells

Koosha Nassiri Nazif,[1†] Alwin Daus,[1†] Jiho Hong,[2,3] Nayeun Lee,[2,3] Sam Vaziri,[1] Aravindh Kumar,[1] Frederick Nitta,[1] Michelle E. Chen,[3] Siavash Kananian,[1] Raisul Islam,[1] Kwan-Ho Kim,[4,5] Jin-Hong Park,[4,6] Ada S. Y. Poon,[1] Mark L. Brongersma,[2,3,7] Eric Pop,[1,3] and Krishna C. Saraswat[1,3*]

[1]Dept. of Electrical Engineering, Stanford University, Stanford, CA 94305, USA

[2]Geballe Laboratory for Advanced Materials, Stanford University, Stanford, CA 94305, USA

[3]Dept. of Materials Science and Engineering, Stanford University, Stanford, CA 94305, USA

[4]Dept. of Electrical and Computer Engineering, Sungkyunkwan University, Suwon 16419, Korea

[5]Dept. of Electrical and Systems Engineering, University of Pennsylvania, Philadelphia, PA 19104, USA

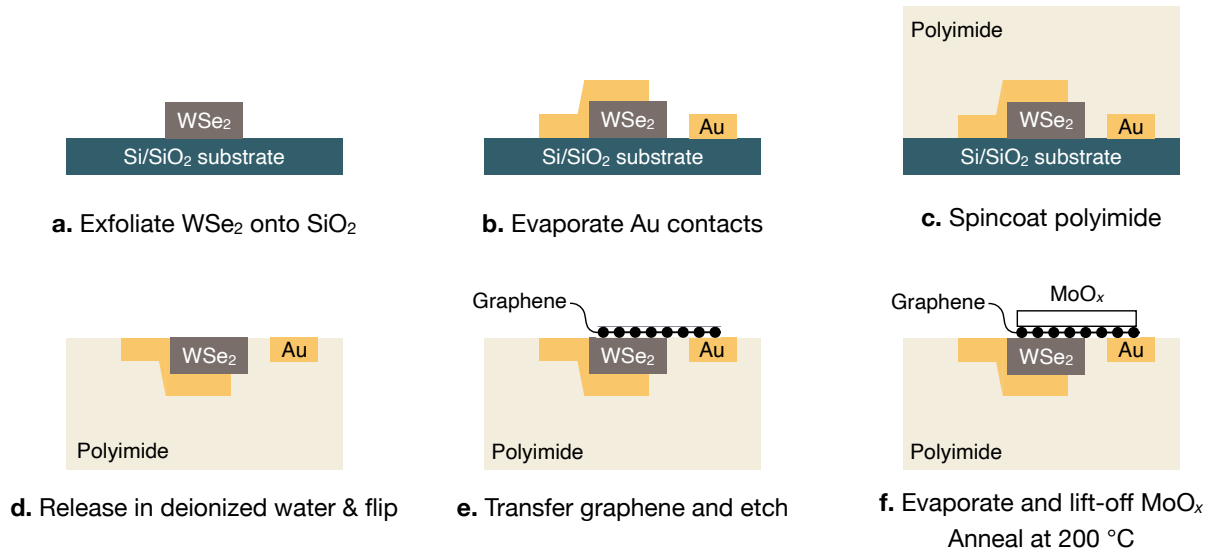[6]SKKU Advanced Inst. of Nanotechnology (SAINT), Sungkyunkwan University, Suwon 16419, Korea

[7]Dept. of Applied Physics, Stanford University, Stanford, CA 94305, USA

[†]These authors contributed equally.

*corresponding author email: saraswat@stanford.edu

**Supplementary Note 1. Detailed fabrication process including transfer procedure**

We follow a recently developed fabrication and transfer approach,[1] where we perform the initial fabrication steps on a rigid Si/SiO₂ substrate followed by the release of patterned electrodes and the transition metal dichalcogenide (TMD) embedded into an ultrathin (~5 μm) flexible polyimide (PI) substrate (Supplementary Fig. 1). This technique is advantageous for vertical device architectures as it eliminates large steps in surface topography leading to a flat surface for the subsequent transfer of transparent graphene top electrodes.



**a.** Exfoliate WSe₂ onto SiO₂    **b.** Evaporate Au contacts    **c.** Spincoat polyimide

**d.** Release in deionized water & flip    **e.** Transfer graphene and etch    **f.** Evaporate and lift-off MoOₓ Anneal at 200 °C

**Supplementary Figure 1 | Flexible solar cell fabrication process**. **a,** Exfoliated WSe₂ flake on Si/SiO₂ substrate. **b,** Deposition of Au bottom contact and contact pads. **c,** Polyimide spin-coating. **d,** Free-standing polyimide substrate (flipped) after release in deionized water as in Ref. 1. **e,** Graphene transfer and etching. **f,** MoOₓ evaporation, patterning and anneal.

The detailed process steps are described below and the summarized process sequence is schematically shown in Supplementary Fig. 1. First, 90 nm of SiO₂ was grown on a bulk silicon wafer by dry thermal oxidation at 1100 °C. The wafers were then manually cut into ~2 cm × 2 cm pieces. Undoped (per manufacturer's description) WSe₂ flakes were mechanically exfoliated from the bulk crystal (2D Semiconductors) onto low-residue thermal release tape (Nitto Denko REVALPHA). They were subsequently transferred from the tape onto the Si/SiO₂ substrate using a WF film (Gel-Film®, WF-20-X4). Next, we spin-coated a lift-off layer LOL 2000 (3000 rpm, 60 s) on our substrates and baked it on a hot plate at 200 °C for 5 minutes. This was followed by spin-coating of Shipley 3612 photoresist (5500 rpm, 30 s) and baking on a hot plate at 90 °C for 1 minute. The lift-off layer/photoresist stack was then patterned by photolithography on a direct write lithography tool (Heidelberg MLA 150, dose:

90 mJ cm$^{-2}$, defocus: -2) and developed (MF-26A, 32 s). 135 nm of Au was deposited on top using electron-beam evaporation (AJA International). After a lift-off process similar as in Ref. 1, patterned Au bottom contacts and metal pads were left behind on top of the flakes and the substrate. The use of Au without any additional sticking layer enables us to later pick up the metal structures and TMD because no covalent bonds with the silicon dioxide substrate are formed (more details in Ref. 1).

The PI (PI-2610, HD MicroSystems) was spin-coated on top of the electrodes and TMD conformally covering all structures, baked at 90 °C and 150 °C for each 90 s, and finally cured at 250 °C in nitrogen ambient for 30 minutes. After that, all structures embedded into PI can be easily released from the silicon substrate by agitation and gentle mechanical force with a tweezer in deionized (DI) water without any discernable damage (more details in Ref. 1). After flipping the substrate, we temporarily attach it again to a silicon carrier with poly(methyl methacrylate) (PMMA) to perform the graphene transfer.

Graphene was grown via chemical vapor deposition at 1060 °C in an AIXTRON Black Magic furnace on commercial Cu foils with large preferentially 100 oriented grains (JX Mining, 99.9% purity HA-V2 treated rolled copper foil), which were surface cleaned in glacial acetic acid and commercial thin film nickel etchant (Transene, Nickel Etchant TFB) solution prior to growth.[2] After growth, the graphene was covered with PMMA via spin-coating (495-A2, 2500 rpm, 60 s, bake 140 °C for 45 s; 950-A4, 2000 rpm, 60 s, bake 80 °C 5 min). The backside of the Cu substrate was reactive ion etched in $O_2$ plasma (Oxford 80 RIE, 20 W, 10 mTorr, 40 sccm, 60 s). Then, the Cu/graphene/PMMA stack was dropped on top of $FeCl_3$ floating on the surface to etch the Cu from the backside. After that the graphene supported by PMMA was transferred by a glass slide into DI water (2 times) followed by diluted $HCl:H_2O_2$ solution (20:1:1 DI water:37% $HCl$:30% $H_2O_2$) and a final DI water beaker staying in each bath for 10 min. Then the graphene/PMMA layer was picked up by the supported PI substrate and the whole stack was allowed to gradually heat to 130 °C on a hotplate for drying. Finally, all PMMA (on top of graphene and below PI) was dissolved in toluene (2 hours) followed by acetone and iso-propanol soaks for each 5 min. To perform optical lithography on the free-standing PI substrates, we attached them to silicon carrier pieces prior to spin-coating with a few drops of photoresist (MEGAPOSIT$^{TM}$ SPR220-3) followed by nitrogen blow drying to flatten the substrate and remove excess photoresist and solvent, which was then baked on a hotplate at 90 °C for 5 minutes. The same photoresist was used for the optical lithography (spin-coating 3000 rpm, 30 s, bake 115 °C 90 s, exposure dose 250 mJ cm$^{-2}$ and defocus -2, post-exposure bake 115 °C for 90 s, develop in MF-26A 75 s). We then etched graphene to remove it in undesired areas by reactive ion etching with the same parameters as mentioned above.

For the purpose of doping, passivation and anti-reflection coating, 10 nm of patterned MoO$_x$ was deposited on top by e-beam evaporation (Kurt J. Lesker) from a MoO$_3$ pellet (Advanced Chemicals, 99.95% purity)

at a rate of 0.3 Å s$^{-1}$, using the same photolithography and lift-off processes as described for the graphene etch and Au contact definition, respectively. Afterwards, we annealed the samples on a hot plate at 200 °C in ambient air for 10 minutes in order to further oxidize MoO$_x$ and therefore increase its work function, resulting in improved surface charge-transfer doping.[3]
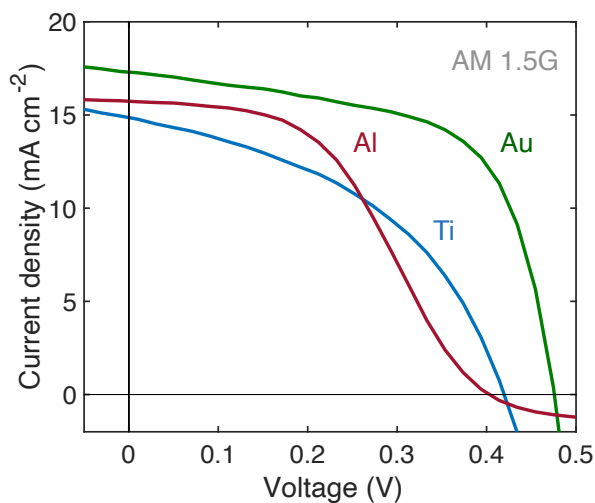
**Supplementary Figure 2 | Performance of flexible WSe$_2$ solar cells having different back contact metals.** Typical *J–V* characteristics of flexible WSe$_2$ solar cells having Al, Ti or Au back contact, under AM 1.5G illumination. Ti and Al, despite their lower work functions compared to Au, lead to worse performance, most probably due to their reactive nature and therefore forming poor interfaces with WSe$_2$. Ti and Al are known to be highly reactive/oxidizing, especially when in contact with TMDs, leading to the formation of AlO$_x$ (~5 nm)[4] at the Al–WSe$_2$ interface and TiO$_x$ + Ti$_x$Se$_y$ at the Ti–WSe$_2$ interface.[5] These defective interfaces result in high levels of charge carrier recombination and therefore decreased open-circuit voltage and short-circuit current. Insulating AlO$_x$ also induces high series resistance as well as a strong roll-over effect in Al-contact solar cells. Note that an AlO$_x$ interlayer with reduced thickness (1-2 nm) could avoid these adverse effects while providing n-type doping as discussed in the manuscript.

**Supplementary Note 2. Doping and passivation effects of MoO$_x$**

The doping/passivation effect of MoO$_x$ on graphene and WSe$_2$ was analyzed by Raman spectroscopy (Supplementary Table 1 and Supplementary Fig. 3a-b). We find small peak shifts towards higher wavenumber for graphene after MoO$_x$ deposition, which has been previously reported to be a result of p-type doping and an increase of graphene's work function.[6] The WSe$_2$ peaks show no clearly discernable changes in peak position given the ~0.3 cm$^{-1}$ detection limit of our Raman instrument, which is similar to the average shifts and standard deviations extracted here. This means that the bulk of WSe$_2$ (probed by Raman) is not affected by MoO$_x$. However, a small interface doping effect due to passivation of trap states at the graphene–WSe$_2$ interface could be associated with the slight red-shift of the Raman peaks.[7,8]

**Supplementary Table 1 | Raman peak shifts upon deposition of MoO$_x$.** A total of 12 spots on several WSe$_2$ flakes were measured. Average Raman peak positions (cm$^{-1}$) for WSe$_2$ and graphene before and after coating with MoO$_x$ are compared in this table showing small peak shifts. The error bar represents the standard deviation.

| Peak | Before MoO$_x$ | After MoO$_x$ |
|---|---|---|
| **Graphene: G** | 1594.0 ± 3.9 | 1597.7 ± 5.9 |
| **Graphene: 2D** | 2689.2 ± 5.2 | 2702.0 ± 3.5 |
| **WSe$_2$: E/A** | 247.0 ± 0.2 | 246.7 ± 0.5 |
| **WSe$_2$: 2LA(M)** | 257.4 ± 0.3 | 257.2 ± 0.3 |

Based on the location of G and 2D peaks in our Raman measurements as well as previous literature reports on graphene doping,[6,9] we estimate carrier densities of ~6.5 × 10$^{12}$ cm$^{-2}$ and ~1.4 × 10$^{13}$ cm$^{-2}$ for air-exposed and MoO$_x$-capped graphene, respectively. The graphene Fermi level (referenced to the Dirac point) and carrier density are related according to the following equation:[10]

$$E_F(n) = \hbar v_F \sqrt{\pi n}$$

where $n$ is the carrier density, $E_F$ is the graphene Fermi level, $\hbar$ is the reduced Planck's constant and $v_F$ is the graphene Fermi velocity (1.15 × 10$^8$ cm s$^{-1}$).[10] Using the above-mentioned carrier density values before and after MoO$_x$ capping, we calculate a Fermi level downshift of 0.16 eV. This increase in Gr work function and therefore Gr–WSe$_2$ built-in potential along with the MoO$_x$ surface passivation effects lead to a $V_{OC}$ improvement of ~50 mV (Supplementary Fig. 3c).
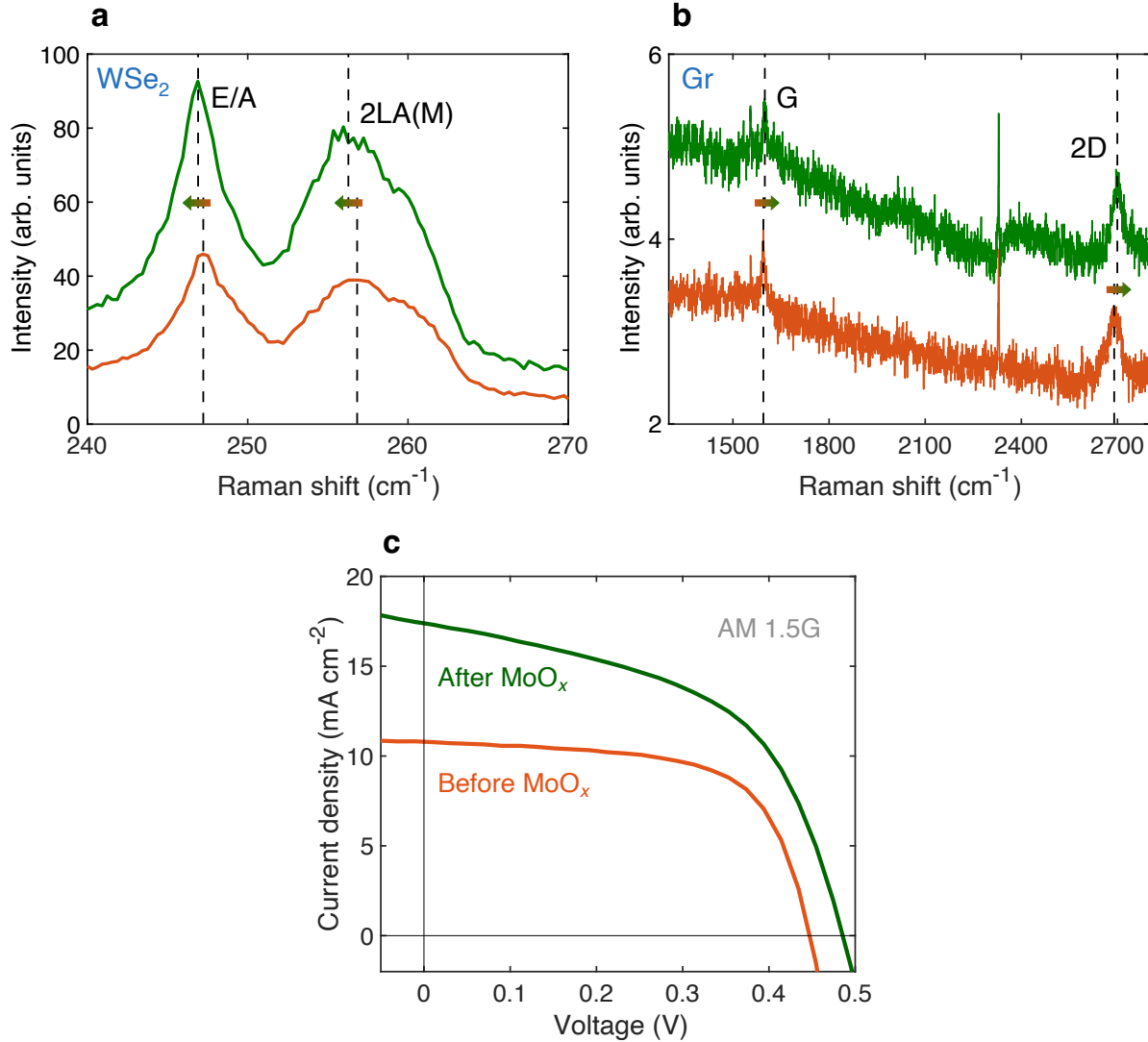
**Supplementary Figure 3 | Performance-improvements by MoO$_x$**. Raman spectroscopy of **a,** WSe$_2$ and **b,** Gr in the Gr–WSe$_2$–Au–PI stack before and after MoO$_x$ deposition. Note, the narrow peak at ~2330 cm$^{-1}$ can be associated with N$_2$ vibrations from ambient air.[11,12] **c,** J–V characteristics of an example Au–WSe$_2$–Gr vertical solar cell before and after 10 nm MoO$_x$ capping. PCE is significantly improved after MoO$_x$ capping due to doping, passivation and anti-reflection effects of MoO$_x$.

We also observe a significant $J_{SC}$ boost of ~60% after 10 nm MoO$_x$ capping (Supplementary Fig. 3c). Our optical simulation (Supplementary Fig. 9d) shows that MoO$_x$ anti-reflection coating is responsible for ~7% of this boost (4.4% $J_{SC}$ improvement). The remaining $J_{SC}$ enhancement can be explained by doping and passivation effects of MoO$_x$ and how they improve the drift length and carrier collection probability.

As discussed in the manuscript, the depletion region covers the entire depth of WSe$_2$. Usually, unity carrier collection probability is assumed for the depletion region, i.e. all photogenerated carriers in the depletion region are collected by the contacts. However, this is not necessarily true for materials like WSe$_2$ that have

a relatively low cross-plane mobility and carrier lifetime. To calculate the collection probability in the depletion region, the concept of drift length (similar to diffusion length) is used, which is directly proportional to the built-in potential and carrier lifetime:[13]

$$L_{drift} = \mu\tau V_{bi}/W$$

where $\mu$ is the carrier mobility, $\tau$ is the carrier lifetime, $V_{bi}$ is the built-in potential, and $W$ is the depletion width (WSe$_2$ thickness in this case). MoO$_x$ capping increases both $V_{bi}$ and $\tau$, and therefore $L_{drift}$; doping graphene p-type and therefore increasing its work function enhances $V_{bi}$, and passivating the top surface of the solar cell improves $\tau$.

Average collection probability (CP) of photogenerated carriers in the depletion region can be estimated by the following equation, where $\alpha$ is the absorption coefficient:[14]

$$CP \approx \frac{\alpha L_{drift}}{1+ \alpha L_{drift}}$$

By increasing $L_{drift}$ via doping and passivation, MoO$_x$ increases the average collection probability and therefore $J_{SC}$, as detailed below.

**Before MoO$_x$ capping:** Assuming a cross-plane WSe$_2$ mobility of 0.01 cm$^2$ V$^{-1}$ s$^{-1}$,[15] a carrier lifetime of 20 ns for unpassivated WSe$_2$,[16] an AM 1.5G-weighted-average absorption coefficient of 0.023 nm$^{-1}$,[17] and a built-in potential of ~0.45 eV, we estimate drift length and collection probability of **45 nm** and **51%**, respectively, which match well with the extracted average internal quantum efficiency (IQE) of **56%**, calculated by dividing the measured $J_{SC}$ (Supplementary Fig. 3c) by maximum attainable $J_{SC}$ derived from optical simulations (Supplementary Fig. 9d).

**After MoO$_x$ capping:** The built-in potential is increased to ~0.61 eV. Carrier lifetimes of up to 611 ns have been reported for multilayer TMDs.[18] Back-calculating from IQE of **87%** (extracted in the same way as above), a drift length of **300 nm** and a lifetime of **98 ns** are estimated.

Therefore the ~56% $J_{SC}$ boost after MoO$_x$ capping (excluding the anti-reflection effect) can be explained by the ~56% improvement in carrier collection probability, caused by the built-in potential increase from ~0.45 V to ~0.61 V (doping effect) and carrier lifetime enhancement from ~20 ns and ~98 ns (passivation effect).

**Supplementary Note 3. Specific power calculation**

The specific power ($P_S$) was calculated based on the solar cell efficiency and the areal weight densities of all materials in the solar cell stack including the PI substrate. Incident power is $P_{in} = 100$ mW cm$^{-2}$, which corresponds to one-sun illumination. We can then calculate the maximum output power $P_{max}$ (unit: mW cm$^{-2}$) as follows:

$$P_{max} = J_{SC} \cdot V_{OC} \cdot FF = PCE \cdot P_{in}$$

where $J_{SC}$, $V_{OC}$, FF and PCE are the short-circuit current density, open-circuit voltage, fill factor and power conversion efficiency, respectively. Then, we sum up the areal mass densities of all materials in the solar cell stack <u>including</u> the substrate by using the volumetric mass density multiplied by the respective material thickness.

**Supplementary Table 2 | Areal mass density of our solar cells**. The volumetric densities of all materials were taken from literature. For MoO$_x$ the volumetric mass density of MoO$_3$ was assumed.

| Peak | PI | Au | WSe$_2$ | Gr | MoO$_x$ | Total |
|---|---|---|---|---|---|---|
| **Thickness (nm)** | 5000 | 135 | 200 | 0.3 | 10 | |
| **Volumetric mass density (g m$^{-3}$)** | $1.4 \times 10^6$ [19] | $1.93 \times 10^7$ [20] | $9.28 \times 10^6$ [21] | $2.27 \times 10^6$ [22] | $4.69 \times 10^6$ [23] | |
| **Areal mass density (g m$^{-2}$)** | 7 | 2.61 | 1.86 | 0.00068 | 0.047 | 11.52 |

We calculate $P_S$ (unit: W g$^{-1}$) by dividing $P_{max}$ by the total area mass density from Supplementary Table 2. With $P_{max} = 5.1$ mW cm$^{-2}$ (see Fig. 1f) we obtain $P_S = 4.4$ W g$^{-1}$. A simple approach to reduce $P_S$ would be thinning down the substrate to ~1 μm, which is the approximate substrate thickness in some of the works with highest $P_S$ achieved so far,[24–26] leading to a value of ~8.6 W g$^{-1}$. A PCE of ~27% can be practically achieved[27] in an optimized TMD single-junction (Supplementary Note 5), further increasing the $P_S$ to ~46 W g$^{-1}$. We included these projections in Fig. 5 to emphasize the great potential of TMDs for high-specific-power photovoltaics.
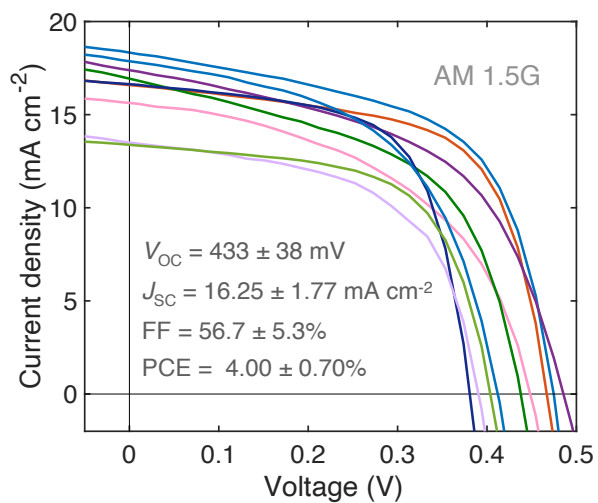
**Supplementary Figure 4 | Reproducibility**. *J–V* measurements of 9 different flexible WSe$_2$ solar cells under AM 1.5G illumination, showing similar characteristics. The numbers represent mean ± standard deviation for each parameter.
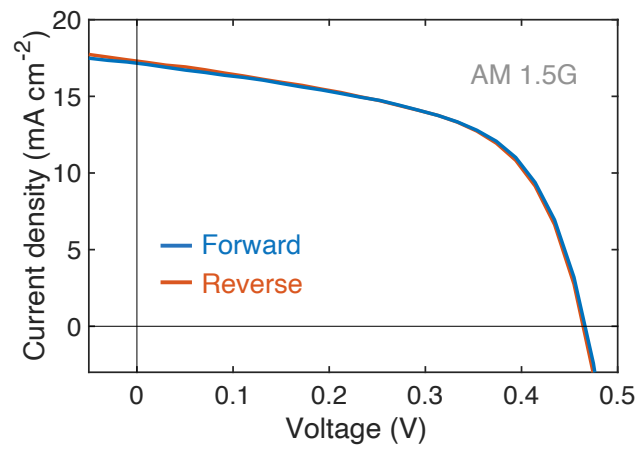
**Supplementary Figure 5 | Forward and backward scans**. J-V characteristics under one-sun illumination show no hysteresis in forward/reverse voltage sweeps.
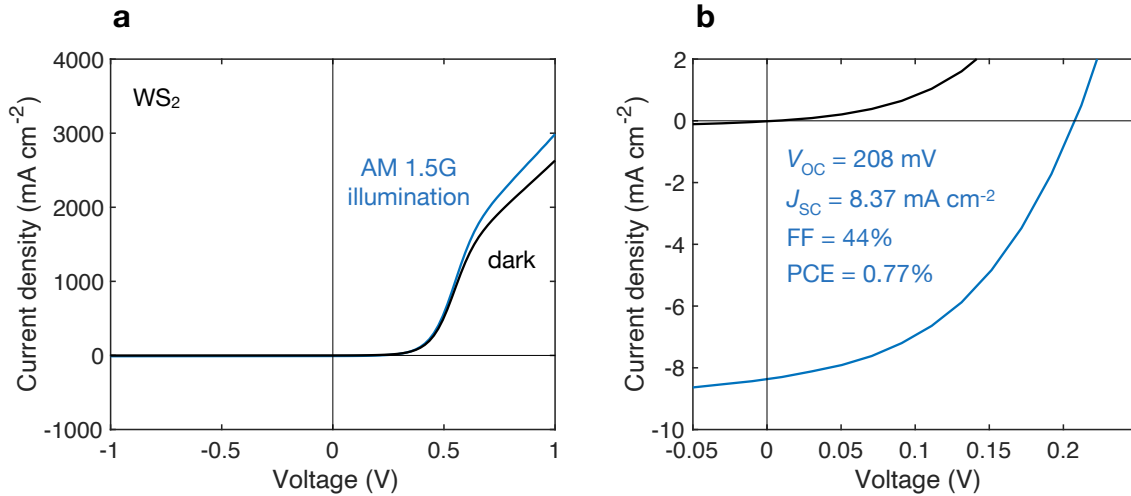
**Supplementary Figure 6 | Flexible WS₂ solar cells**. **a-b,** $J$–$V$ characteristics of flexible WS₂ solar cells having the exact same design as WSe₂ cells discussed in the main text (Fig. 1b), in dark and under one-sun illumination. **b,** a zoom-in view of the photovoltaic region. WS₂ solar cells show the same $J$–$V$ characteristics as WSe₂ cells, however with lower performance. Similar to WSe₂, Au pins near the midgap of WS₂.[28] Given the higher electron affinity and bandgap in WS₂,[29] this leads to a smaller built-in potential and therefore reduced $V_{OC}$, $J_{SC}$, and FF in fully depleted Gr–WS₂–Au solar cells. Further p-doping Gr (for example by using flame-deposited MoO₃)[6] is one way to achieve a similar built-in potential and therefore performance in WS₂ solar cells.

$$R_{SH} = \beta \cdot (P_{in})^{\alpha}$$

$$\alpha = -0.88$$
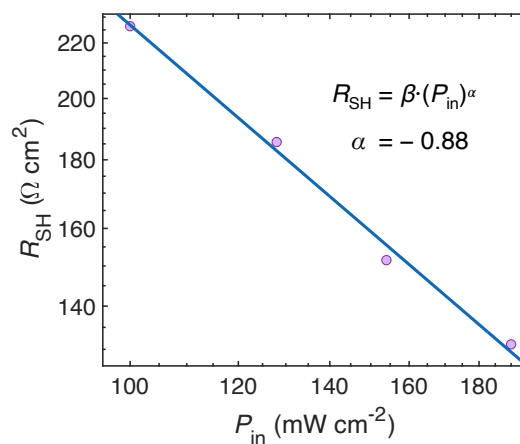
**Supplementary Figure 7 | Photoshunting**. Shunt resistance ($R_{SH}$) of a typical flexible WSe$_2$ solar cell at various incident power ($P_{in}$) intensities of AM 1.5G illumination. Shunt resistance decreases almost linearly with increasing incident power intensity due to increased minority carrier conductivity across the device under illumination, a phenomenon known as photoshunting.[30,31] Utilizing contacts with greater carrier selectivity or introducing a high built-in potential p-n homojunction could reduce or eliminate the photoshunting observed here. Symbols, measurements; line, power law fit.
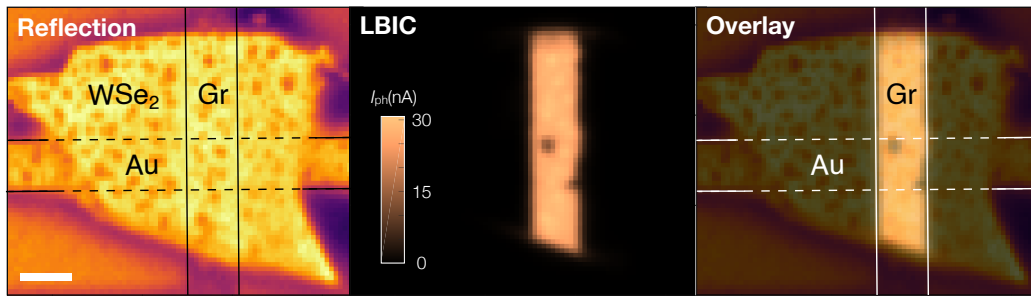
**Supplementary Figure 8 | Photocurrent mapping.** Spatial maps of reflection, photocurrent, and reflection/photocurrent overlay for a flexible Au–WSe$_2$–Gr solar cell measured at λ = 530 nm. Current generation occurs only in the WSe$_2$ region under the Gr contact, which can be used to accurately define the active area of the solar cell. No photocurrent generation is observed at the Au–WSe$_2$ back diode. Scale bar, 10 μm.
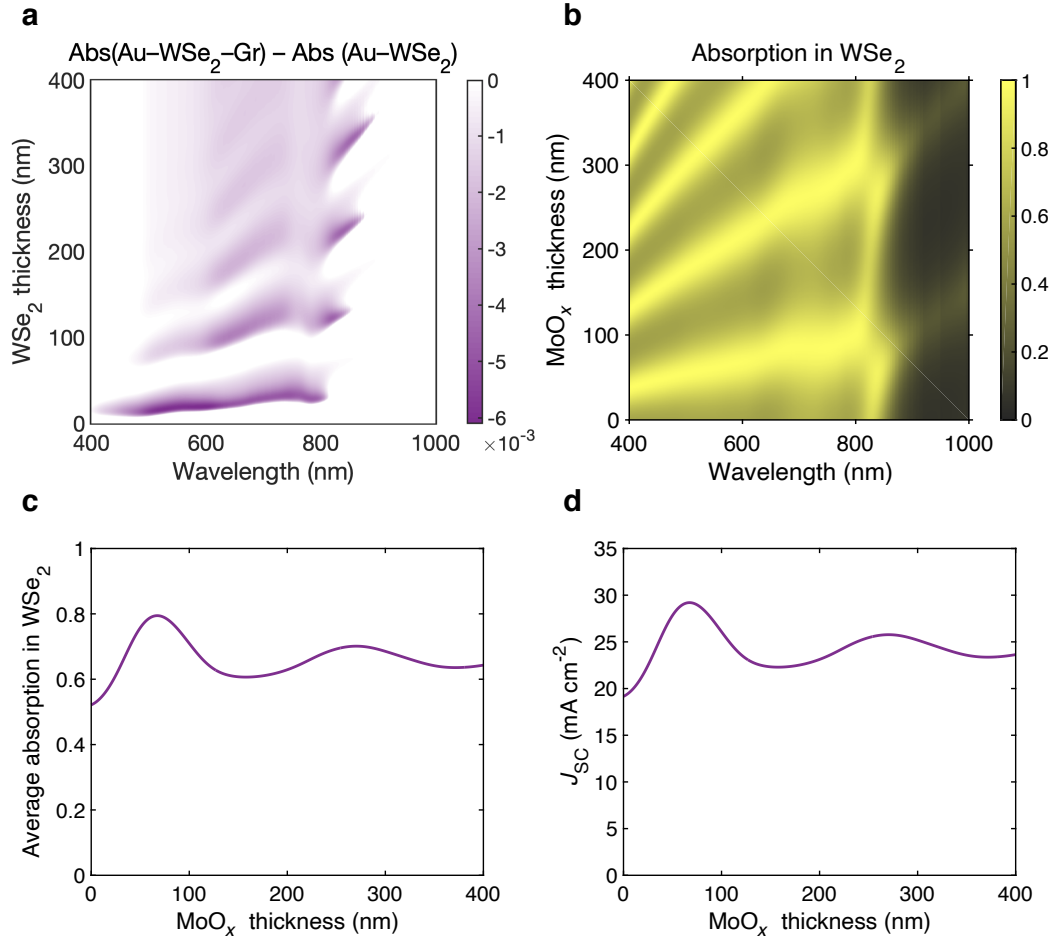
**Supplementary Figure 9 | Effects of Gr and MoO$_x$ on optical absorption. a,** Absorption reduction by graphene. The difference in total absorption between the Au–WSe$_2$ and Au–WSe$_2$–Gr stacks, showing that adding graphene on top slightly reduces the total absorption in the ~500–800 nm wavelength spectrum for WSe$_2$ thicknesses around 200 nm, in agreement with experimental measurements (Fig. 3c). **b–d,** Anti-reflection coating effects of MoO$_x$. **b,** Absorption spectrum and **c,** average absorption of WSe$_2$ in the Au–WSe$_2$–Gr–MoO$_x$ stack as a function of MoO$_x$ thickness. WSe$_2$ thickness is 209 nm, similar to the device in Fig. 3c. **d,** Maximum short-circuit current density ($J_{SC}$) attainable from WSe$_2$ in the same stack, as a function of MoO$_x$ thickness, calculated by integrating Absorption($\lambda$) × (spectral photon flux of AM1.5G spectrum at one-sun solar intensity) over the wavelength range of $\lambda$ = 400–1000 nm, assuming unity internal quantum efficiency (IQE). This maximum $J_{SC}$ value is slightly underestimated as absorption at wavelengths below 400 nm and above 1000 nm are not included due to lack of material data. An optimal MoO$_x$ thickness of ~70 nm can increase the average absorption in WSe$_2$ and similarly $J_{SC}$ by ~50%, leading to a remarkable ~80% average absorption and ~30 mA cm$^{-2}$ $J_{SC}$ in WSe$_2$ solar cells.

15

**Supplementary Note 4. Benchmarking**

We performed an extensive literature review on flexible and light-weight solar cells with various absorber materials and calculated $P_S$ based on information provided. Some works directly stated $P_S$ or at least PCE and the areal mass density, while others did not explicitly provide information on the weight of their solar cells. In some cases, we calculated the weight based on the substrate and the solar cell layer stack if the substrate weight was small (sufficiently thin/low density substrate material) and therefore the weight of other materials was non-negligible. In other cases, we only used the substrate weight for estimating $P_S$ if it appeared to dominate (thicker high-density substrate materials) and neglected the weight of other materials. Supplementary Table 3 lists all the works shown in Fig. 5 indicating how $P_S$ was obtained.

**Supplementary Table 3 | Literature reports on flexible and light-weight solar cells with notable specific power ($P_S$), along with their power conversion efficiencies (PCE)**. Unmarked $P_S$ is directly taken from the literature reports. *$P_S$ calculated based on the solar cell layer stack including the substrate. **$P_S$ calculated only based on substrate weight or absorber material if free-standing. ***PCE corresponds to performance under AM 0 illumination (space).

| Reference | Technology | PCE (%) | $P_S$ (W g$^{-1}$) |
|---|---|---|---|
| Kaltenbrunner et al.[32] | Perovskite | 12 | 23 |
| Kaltenbrunner et al.[33] | Organic | 4 | 10 |
| Söderström et al.[34] | Amorphous Si (a-Si) | 8.8 | 3.3 |
| Chirilă et al.[35] | CuInGaSe (CIGS) | 18.7 | 3.3 |
| Shiu et al.[36] | InP (III-V) | 10.2 | 2.0 |
| Romeo et al.[37] | CdTe (II-VI) | 11.4 | 2.1 |
| Fatemi et al.[38] | 3-mil Si (c-Si) | 17*** | 0.85 |
| Fatemi et al.[38] | InGaP/GaAs/Ge (III-V) | 26*** | 0.4 |
| Zhao et al.[39] | Single-crystal Si (c-Si) | 24.4 | 0.4 |
| Zhao et al.[39] | Polycrystalline Si (poly-Si) | 19.8 | 0.33 |
| Bremaud et al.[40] | CuInGaSe (CIGS) | 15 | 0.09 |
| Kang et al.[24] | Perovskite | 12.85 | 29.4 |
| Zhang et al.[25] | PbS quantum dot | 9.9 | 15.2 |
| Liu et al.[41] | Perovskite | 11.5 | 5 |
| Lin et al.[42] | Amorphous Si (a-Si) | 7.06 | 0.5** |
| Park et al.[26] | Organic | 10.5 | 11.46 |

| Reference | Technology | PCE (%) | $P_S$ (W g$^{-1}$) |
|---|---|---|---|
| Tavakoli et al.[43] | PbS quantum dot | 7.1 | 12.3 |
| Li et al.[44] | Perovskite | 13 | 3.7** |
| Jinno et al.[45] | Organic | 7.9 | 14* |
| Jia et al.[46] | Perovskite | 18 | 1.3** |
| Lee et al.[47] | Perovskite | 17.03 | 18.5* |
| Cardwell et al.[48] | GaInP/GaAs/GaInAs (III-V) | 29.3*** | 3.8 |
| Xie et al.[49] | Perovskite | 13.32 | 4.16 |
| Sun et al.[50] | Amorphous Si (a-Si) | 5.6 | 1.382 |
| Başol et al.[51] | CuInSe$_2$ (CIS) | 9.3 | 1.133 |
| Rance et al.[52] | CdTe (II-VI) | 14.05 | 0.6** |
| Mahabaduge et al.[53] | CdTe (II-VI) | 16.4 | 0.7** |
| Law et al.[54] | GaInP/GaInAs/Ge (III-V) | 21*** | 2.067 |
| Kim et al.[55] | GaAs (III-V) | 15.2 | 5.9* |
| Gerthoffer et al.[56] | Cu(In,Ga)Se$_2$ (CIGS) | 11.2 | 0.4** |
| Jeong et al.[57] | Single-crystal Si (c-Si) | 13.7 | 5.88** |
| Das et al.[58] | Single-crystal Si (c-Si) | 9 | 1.89 |
| Hwang et al.[59] | Single-crystal Si (c-Si) | 18.4 | 1.3* |
| Jean et al.[60] | Organic | 2.2 | 6.11 |
| Salavei et al.[61] | CdTe (II-VI) | 10 | 1.98 |
| Shahrjerdi et al.[62] | InGaP/(In)GaAs (III-V) | 28.1 | 1.995 |
| Cho et al.[63] | CdS/CdTe (II-VI) | 13.56 | 0.254 |
| Zhao et al.[64] | Organic | 8.7 | 0.4 |
| Li et al.[65] | Perovskite | 14 | 1.96 |
| Romeo et al.[66] | CdTe/CdS (II-VI) | 11 | 2.6* |
| Liu et al.[67] | Organic | 6.62 | 1.71 |
| Chirilă et al.[68] | Cu(In,Ga)Se$_2$ (CIGS) | 20.4 | 3.4* |
| Xu et al.[69] | Amorphous Si (a-Si) | 9.7*** | 1.2 |
| Mavlonov et al.[70] | Cu(In,Ga)Se$_2$ (CIGS) | 9.1 | 0.7* |
| Qu et al.[71] | Organic | 16.1 | 11.5** |
| Koo et al.[72] | Organic | 15.2 | 10.8** |
| Garud et al.[73] | Polycrystalline Si (poly-Si) | 15 | 0.06** |
| El-Atab et al.[74] | Single-crystal Si (c-Si) | 19.1 | 0.24 |

| Reference | Technology | PCE (%) | $P_S$ (W g$^{-1}$) |
|-----------|-----------|---------|--------------------|
| Augusto et al.[75] | Single-crystal Si (c-Si) | 18.4 | 1.3** |
| Lee et al.[76] | Single-crystal Si (c-Si) | 12.4 | 1* |
| El-Atab et al.[77] | Single-crystal Si (c-Si) | 19 | 0.29 |
| Xue et al.[78] | Single-crystal Si (c-Si) | 12.3 | 9.33* |
| Tanabe et al.[79] | InAs/GaAs quantum dot (III-V) | 10.5 | 0.6** |
| Wu et al.[80] | Dye-Sensitized (DSSC) | 6.69 | 0.3** |
| Akama et al.[81] | WS$_2$ (TMD) | <0.7% | <0.04** |

**Supplementary Note 5. Realistic efficiency limits of WSe$_2$ solar cells**

We performed realistic detailed balance calculations to determine the efficiency limits of ultrathin WSe$_2$ solar cells which can be achieved in practice with an optimized optical and electronic design. We started by the ideal Shockley–Queisser model[82] where all photons with energies above the band gap energy are absorbed and the only recombination mechanism is radiative, leading to an idealistic 33.4% efficiency limit.

Next, we adopted the more advanced Tiedje–Yablonovitch model,[83] where the measured spectral absorption coefficient of the absorber layer (WSe$_2$)[17] is used to calculate both absorption and radiative recombination. The model also includes free carrier absorption and Auger recombination (data from Ref. 84) in addition to radiative losses. This leads to a lower, more realistic efficiency limit which is dependent on the thickness of the absorber layer.

Lastly, we added the defect-assisted Shockley-Read-Hall (SRH) recombination to the Tiedje–Yablonovitch model to account for the varying material quality of TMDs, which is correlated with SRH recombination lifetime ($\tau_{SRH}$); the higher the SRH lifetime, the higher the material quality. SRH lifetimes of up to 611 ns have been reported for multilayer TMDs, which, according to our calculations, corresponds to a realistic efficiency limit of ~27% occurring at a WSe$_2$ thickness of ~110 nm (Supplementary Fig. 10).
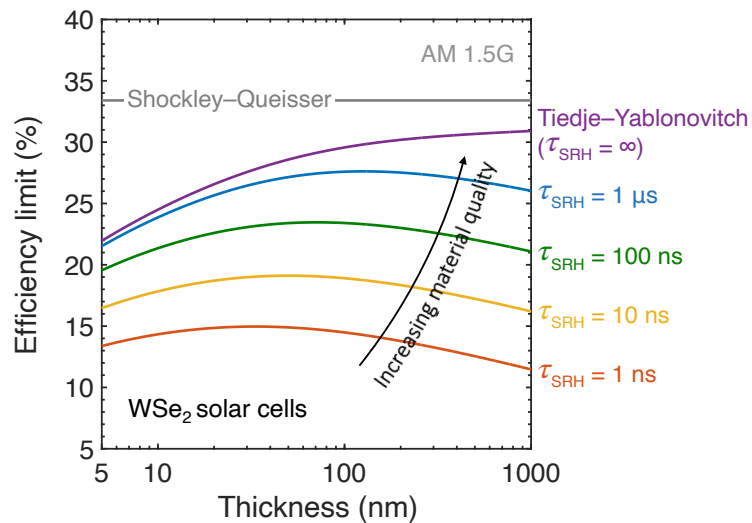


**Supplementary Figure 10 | Efficiency limits of WSe$_2$ solar cells.** Shockley–Queisser, Tiedje–Yablonovitch and modified Tiedje–Yablonovitch (including SRH recombination) efficiency limits of WSe$_2$ solar cells under AM 1.5G illumination. The realistic modified Tiedje–Yablonovitch model reveals maximum efficiencies practically attainable in ultrathin WSe$_2$ solar cells at different material quality levels (SRH lifetimes, $\tau_{SRH}$) and their corresponding optimal thicknesses. SRH lifetimes of up to 611 ns have been reported for multilayer TMDs,[18] leading to a maximum efficiency of ~27% at an optimal thickness of ~110 nm.

**Supplementary References:**

1.  Daus, A. *et al.* High-performance flexible nanoscale transistors based on transition metal dichalcogenides. *Nat. Electron.* **4,** 495–501 (2021).

2.  Chen, M. E. *et al.* Graphene-based electromechanical thermal switches. *2D Mater*. **8,** 035055 (2021).

3.  Ishikawa, R. *et al.* Effect of annealing on doping of graphene with molybdenum oxide. *Appl. Phys. Express* **11**, 45101 (2018).

4.  Lu, C.-C., Lin, Y.-C., Yeh, C.-H., Huang, J.-C. & Chiu, P.-W. High mobility flexible graphene field-effect transistors with self-healing gate dielectrics. *ACS Nano* **6**, 4469–4474 (2012).

5.  Schauble, K. *et al.* Uncovering the effects of metal contacts on monolayer $MoS_2$. *ACS Nano* **14**, 14798–14808 (2020).

6.  Vaziri, S. *et al.* Ultrahigh doping of graphene using flame-deposited $MoO_3$. *IEEE Electron Device Lett.* **41**, 1592–1595 (2020).

7.  Nassiri Nazif, K. *et al.* High-performance p–n junction transition metal dichalcogenide photovoltaic cells enabled by $MoO_x$ doping and passivation. *Nano Lett.* **21**, 3443–3450 (2021).

8.  Cai, L. *et al.* Rapid flame synthesis of atomically thin $MoO_3$ down to monolayer thickness for effective hole doping of $WSe_2$. *Nano Lett.* **17**, 3854–3861 (2017).

9.  Das, A. *et al.* Monitoring dopants by Raman scattering in an electrochemically top-gated graphene transistor. *Nat. Nanotechnol.* **3**, 210–215 (2008).

10. Kim, S. *et al.* Direct measurement of the Fermi energy in graphene using a double-layer heterostructure. *Phys. Rev. Lett.* **108**, 116404 (2012).

11. Huang, N. *et al.* Full range characterization of the Raman spectra of organs in a murine model. *Opt. Express* **19**, 22892–22909 (2011).

12. Spizzirri, P. G., Fang, J.-H., Rubanov, S., Gauja, E. & Prawer, S. Nano-Raman spectroscopy of silicon surfaces. (2010).

13. Johnston, K. W. *et al.* Efficient Schottky-quantum-dot photovoltaics: the roles of depletion, drift, and diffusion. *Appl. Phys. Lett.* **92**, 122111 (2008).

14. Li, S. S. *Semiconductor Physical Electronics* (Springer, New York, 2006)

15. Massicotte, M. *et al.* Picosecond photoresponse in van der Waals heterostructures. *Nat. Nanotechnol.* **11**, 42–46 (2016).

16. Jakubowicz, A., Mahalu, D., Wolf, M., Wold, A. & Tenne, R. $WSe_2$: optical and electrical properties as related to surface passivation of recombination centers. *Phys. Rev. B* **40**, 2992–3000 (1989).

17. Kravets, V. G. Ellipsometry and optical spectroscopy of low-dimensional family TMDs. *Semicond. Phys. Quantum Electron. Optoelectron.* **20**, 284–296 (2017).

18. Went, C. M. *et al.* A new metal transfer process for van der Waals contacts to vertical Schottky-junction transition metal dichalcogenide photovoltaics. *Sci. Adv.* **5**, eaax6061 (2019).

19. Density of polyimide. Available at: https://www.yumpu.com/fr/document/view/2032698/pi-2600-series-low-stress-applications-hd-microsystems.

20. Density of gold (Au). Available at: http://chemistry.elmhurst.edu/vchembook/125Adensitygold.html.

21. Agarwal, M. K. & Wani, P. A. Growth conditions and crystal structure parameters of layer compounds in the series $Mo_{1-x}W_xSe_2$. *Mater. Res. Bull.* **14**, 825–830 (1979).

22. Density of graphene (Gr). Available at: https://www.americanelements.com/graphene-1034343-98-0.

23. Density of molybdenum trioxide ($MoO_3$). Available at: https://pubchem.ncbi.nlm.nih.gov/compound/Molybdenum-trioxide.

24. Kang, S. *et al.* Ultrathin, lightweight and flexible perovskite solar cells with an excellent power-per-weight performance. *J. Mater. Chem. A* **7**, 1107–1114 (2019).

25. Zhang, X., Öberg, V. A., Du, J., Liu, J. & Johansson, E. M. J. Extremely lightweight and ultra-flexible infrared light-converting quantum dot solar cells with high power-per-weight output using a solution-processed bending durable silver nanowire-based electrode. *Energy Environ. Sci.* **11**, 354–364 (2018).

26. Park, S. *et al.* Self-powered ultra-flexible electronics via nano-grating-patterned organic photovoltaics. *Nature* **561**, 516–521 (2018).

27. Jariwala, D., Davoyan, A. R., Wong, J. & Atwater, H. A. Van der Waals materials for atomically-thin photovoltaics: promise and outlook. *ACS Photonics* **4**, 2962–2970 (2017).

28. Park, W. *et al.* Complementary unipolar $WS_2$ field-effect transistors using Fermi-level depinning layers. *Adv. Electron. Mater.* **2**, 1500278 (2016).

29. Guo, Y. & Robertson, J. Band engineering in transition metal dichalcogenides: stacked versus lateral heterostructures. *Appl. Phys. Lett.* **108**, 233104 (2016).

30. Waldauf, C., Scharber, M. C., Schilinsky, P., Hauch, J. A. & Brabec, C. J. Physics of organic bulk heterojunction devices for photovoltaic applications. *J. Appl. Phys.* **99**, 104503 (2006).

31. Würfel, U., Cuevas, A. & Würfel, P. Charge carrier separation in solar cells. *IEEE J. Photovoltaics* **5**, 461–469 (2015).

32. Kaltenbrunner, M. *et al.* Flexible high power-per-weight perovskite solar cells with chromium oxide–metal contacts for improved stability in air. *Nat. Mater.* **14**, 1032–1039 (2015).

33. Kaltenbrunner, M. *et al.* Ultrathin and lightweight organic solar cells with high flexibility. *Nat. Commun.* **3**, 770 (2012).

34. Söderström, T., Haug, F.-J., Terrazzoni-Daudrix, V. & Ballif, C. Optimization of amorphous silicon thin film solar cells for flexible photovoltaics. *J. Appl. Phys.* **103**, 114509 (2008).

35. Chirilă, A. *et al.* Highly efficient Cu(In,Ga)Se$_2$ solar cells grown on flexible polymer films. *Nat. Mater.* **10**, 857–861 (2011).

36. Shiu, K.-T., Zimmerman, J., Wang, H. & Forrest, S. R. Ultrathin film, high specific power InP solar cells on flexible plastic substrates. *Appl. Phys. Lett.* **95**, 223503 (2009).

37. Romeo, A. *et al.* High-efficiency flexible CdTe solar cells on polymer substrates. *Sol. Energy Mater. Sol. Cells* **90**, 3407–3415 (2006).

38. Fatemi, N. S., Pollard, H. E., Hou, H. Q. & Sharps, P. R. Solar array trades between very high-efficiency multi-junction and Si space solar cells. in *Conference Record of the Twenty-Eighth IEEE Photovoltaic Specialists Conference - 2000 (Cat. No.00CH37036)* 1083–1086 (2000).

39. Zhao, J., Wang, A., Green, M. A. & Ferrazza, F. 19.8% efficient "honeycomb" textured multicrystalline and 24.4% monocrystalline silicon solar cells. *Appl. Phys. Lett.* **73**, 1991–1993 (1998).

40. Bremaud, D., Rudmann, D., Bilger, G., Zogg, H. & Tiwari, A. N. Towards the development of flexible CIGS solar cells on polymer films with efficiency exceeding 15%. in *Conference Record of the Thirty-first IEEE Photovoltaic Specialists Conference, 2005.* 223–226 (2005).

41. Liu, Z., You, P., Xie, C., Tang, G. & Yan, F. Ultrathin and flexible perovskite solar cells with graphene transparent electrodes. *Nano Energy* **28**, 151–157 (2016).

42. Lin, Q. *et al.* High performance thin film solar cells on plastic substrates with nanostructure-enhanced flexibility. *Nano Energy* **22**, 539–547 (2016).

43. Tavakoli, M. M. *et al.* Efficient, flexible, and ultra-lightweight inverted PbS quantum dots solar cells on all-CVD-growth of parylene/graphene/oCVD PEDOT substrate with high power-per-weight. *Adv. Mater. Interfaces* **7**, 2000498 (2020).

44. Li, H. *et al.* Ultraflexible and biodegradable perovskite solar cells utilizing ultrathin cellophane paper substrates and TiO$_2$/Ag/TiO$_2$ transparent electrodes. *Sol. Energy* **188**, 158–163 (2019).

45. Jinno, H. *et al.* Stretchable and waterproof elastomer-coated organic photovoltaics for washable electronic textile applications. *Nat. Energy* **2**, 780–785 (2017).

46. Jia, C. *et al.* Highly flexible, robust, stable and high efficiency perovskite solar cells enabled by van der Waals epitaxy on mica substrate. *Nano Energy* **60**, 476–484 (2019).

47. Lee, G. *et al.* Ultra-flexible perovskite solar cells with crumpling durability: toward a wearable power source. *Energy Environ. Sci.* **12**, 3182–3191 (2019).

48. Cardwell, D. *et al.* Very high specific power ELO solar cells (>3 kW/kg) for UAV, space, and portable power applications. in *2017 IEEE 44th Photovoltaic Specialist Conference (PVSC)* 3511–

3513 (2017).

49. Xie, M. *et al.* Super-flexible perovskite solar cells with high power-per-weight on 17 μm thick PET substrate utilizing printed Ag nanowires bottom and top electrodes. *Flex. Print. Electron.* **4**, 34002 (2019).

50. Sun, X. *et al.* Firmly standing three-dimensional radial junctions on soft aluminum foils enable extremely low cost flexible thin film solar cells with very high power-to-weight performance. *Nano Energy* **53**, 83–90 (2018).

51. Başol, B. M., Kapur, V. K., Leidholm, C. R., Halani, A. & Gledhill, K. Flexible and light weight copper indium diselenide solar cells on polyimide substrates. *Sol. Energy Mater. Sol. Cells* **43**, 93–98 (1996).

52. Rance, W. L. *et al.* 14%-efficient flexible CdTe solar cells on ultra-thin glass substrates. *Appl. Phys. Lett.* **104**, 143903 (2014).

53. Mahabaduge, H. P. *et al.* High-efficiency, flexible CdTe solar cells on ultra-thin glass substrates. *Appl. Phys. Lett.* **106**, 133501 (2015).

54. Law, D. C. *et al.* Lightweight, flexible, high-efficiency III-V multijunction cells. in *2006 IEEE 4th World Conference on Photovoltaic Energy Conference* **2**, 1879–1882 (2006).

55. Kim, J. *et al.* Ultra-thin flexible GaAs photovoltaics in vertical forms printed on metal surfaces without interlayer adhesives. *Appl. Phys. Lett.* **108**, 253101 (2016).

56. Gerthoffer, A. *et al.* CIGS solar cells on flexible ultra-thin glass substrates: characterization and bending test. *Thin Solid Films* **592**, 99–104 (2015).

57. Jeong, S., McGehee, M. D. & Cui, Y. All-back-contact ultra-thin silicon nanocone solar cells with 13.7% power conversion efficiency. *Nat. Commun.* **4**, 2950 (2013).

58. Das, S. *et al.* A leaf-inspired photon management scheme using optically tuned bilayer nanoparticles for ultra-thin and highly efficient photovoltaic devices. *Nano Energy* **58**, 47–56 (2019).

59. Hwang, I. *et al.* Effective photon management of non-surface-textured flexible thin crystalline silicon solar cells. *Cell Reports Phys. Sci.* **1**, 100242 (2020).

60. Jean, J., Wang, A. & Bulović, V. In situ vapor-deposited parylene substrates for ultra-thin, lightweight organic solar cells. *Org. Electron.* **31**, 120–126 (2016).

61. Salavei, A. *et al.* Flexible CdTe solar cells on polyimide and flexible glass substrates. *Proc. EU PVSEC 2015* 1356–1357 (2015).

62. Shahrjerdi, D. *et al.* Ultralight high-efficiency flexible InGaP/(In)GaAs tandem solar cells on plastic. *Adv. Energy Mater.* **3**, 566–571 (2013).

63. Cho, E., Kang, Y., Kim, D. & Kim, J. Post-growth process for flexible CdS/CdTe thin film solar cells with high specific power. *Opt. Express* **24**, A791–A796 (2016).

64. Zhao, B. *et al.* Flexible polymer solar cells with power conversion efficiency of 8.7%. *J. Mater. Chem. C* **2**, 5077–5082 (2014).

65. Li, Y. *et al.* High-efficiency robust perovskite solar cells on ultrathin flexible substrates. *Nat. Commun.* **7**, 10214 (2016).

66. Romeo, A., Arnold, M., Bätzner, D. L., Zogg, H. & Tiwari, A. N. Development of high efficiency flexible solar cells. in *PV in Europe - From PV Technology to Energy Solutions* **1**, 377–381 (2002).

67. Liu, Y. *et al.* Highly flexible and lightweight organic solar cells on biocompatible silk fibroin. *ACS Appl. Mater. Interfaces* **6**, 20670–20675 (2014).

68. Chirilă, A. *et al.* Potassium-induced surface modification of Cu(In,Ga)Se$_2$ thin films for high-efficiency solar cells. *Nat. Mater.* **12**, 1107–1111 (2013).

69. Xu, X. *et al.* High efficiency ultra lightweight a-Si:H/a-SiGe:H/a-SiGe:H triple-junction solar cells on polymer substrate using roll-to-roll technology. in *2008 33rd IEEE Photovoltaic Specialists Conference* 1–6 (2008).

70. Mavlonov, A. *et al.* Superstrate-type flexible and bifacial Cu(In,Ga)Se$_2$ thin-film solar cells with In$_2$O$_3$:SnO$_2$ back contact. *Sol. Energy* **211**, 725–731 (2020).

71. Qu, T.-Y. *et al.* Biomimetic electrodes for flexible organic solar cells with efficiencies over 16%. *Adv. Opt. Mater.* **8**, 2000669 (2020).

72. Koo, D. *et al.* Flexible organic solar cells over 15% efficiency with polyimide-integrated graphene Electrodes. *Joule* **4**, 1021–1034 (2020).

73. Garud, S. *et al.* Toward high solar cell efficiency with low material usage: 15% efficiency with 14 µm polycrystalline silicon on glass. *Sol. RRL* **4**, 2000058 (2020).

74. El-Atab, N., Shamsuddin, R., Bahabry, R. & Hussain, M. M. High-Efficiency corrugated monocrystalline silicon solar cells with multi-directional flexing capabilities. in *2019 IEEE 46th Photovoltaic Specialists Conference (PVSC)* 1499–1501 (2019).

75. Augusto, A., Tyler, K., Herasimenka, S. Y. & Bowden, S. G. Flexible modules using <70 µm thick silicon solar cells. *Energy Procedia* **92**, 493–499 (2016).

76. Lee, S.-M. *et al.* Printable nanostructured silicon solar cells for high-performance, large-area flexible photovoltaics. *ACS Nano* **8**, 10507–10516 (2014).

77. El-Atab, N., Khan, S. M. & Hussain, M. M. Flexible high-efficiency corrugated monocrystalline silicon solar cells for application in small unmanned aerial vehicles for payload transportation. *Energy Technol.* **8**, 2000670 (2020).

78. Xue, M. *et al.* Free-standing 2.7 µm thick ultrathin crystalline silicon solar cell with efficiency above 12.0%. *Nano Energy* **70**, (2020).

79. Tanabe, K., Watanabe, K. & Arakawa, Y. Flexible thin-film InAs/GaAs quantum dot solar cells.

*Appl. Phys. Lett.* **100**, 192102 (2012).

80. Wu, J. *et al.* A Large-area light-weight dye-sensitized solar cell based on all titanium substrates with an efficiency of 6.69% outdoors. *Adv. Mater.* **24**, 1884–1888 (2012).

81. Akama, T. *et al.* Schottky solar cell using few-layered transition metal dichalcogenides toward large-scale fabrication of semitransparent and flexible power generator. *Sci. Rep.* **7**, 11967 (2017).

82. Shockley, W. & Queisser, H. J. Detailed balance limit of efficiency of p-n junction solar cells. *J. Appl. Phys.* **32**, 510–519 (1961).

83. Tiedje, T., Yablonovitch, E., Cody, G. D. & Brooks, B. G. Limiting efficiency of silicon solar cells. *IEEE Trans. Electron Devices* **31**, 711–716 (1984).

84. Piprek, J. Efficiency droop in nitride-based light-emitting diodes. *Phys. status solidi* **207**, 2217–2225 (2010).